Reiwa 3rd Doctor Thesis

Pressure effect on electric and magnetic properties in λ-$(D)_2GaCl_4$ [D = ET, BETS] proved by ^{13}C-NMR and Coupling of molecular motion and electronic state of organic molecular dimer Mott insulator β'-$(ET)_2ICl_2$ proved by ^{1}H- and ^{13}C-NMR

(^{13}C-NMR 法による、λ-$(D)_2GaCl_4$ [D = ET, BETS] の圧力下電子物性の研究
および
^{1}H- および ^{13}C-NMR 法による、ダイマー Mott 絶縁体 β'-$(ET)_2ICl_2$ の電子状態と結合する分子運動に関する研究)

Masashi Sawada[1]

[1]Low-temperature physics group, Department of Condensed Matter Physics,
Graduate School of Science, Hokkaido University

March, 2021

Contents

I Pressure effect on electric and magnetic properties in λ-$(ET)_2GaCl_4$ proved by ^{13}C-NMR **5**

1 Introduction 5
- 1.1 General characteristics of ET-based organic conductors 5
- 1.2 Role of organic conductors 8
- 1.3 λ-$(D)_2GaCl_4$ [D = ET, STF, BETS] 10
- 1.4 Physical properties of λ-$(ET)_2GaCl_4$ 12
- 1.5 Physical properties of λ-$(STF)_2GaCl_4$ 13

2 Motivation 14

3 Experiments 15
- 3.1 Sample preparation and settings 15
- 3.2 Sample identification 15
- 3.3 Condition of NMR measurement 15

4 Results and Discussion 18
- 4.1 NMR spectra and $1/T_1T$ 18
- 4.2 NMR shift 19
- 4.3 Difficulty in λ-$(ET)_2GaCl_4$ 19
- 4.4 Alternate options 21

5 Summary for Part. I 24

II Enhancement of electron correlation and SDW fluctuations under pressure of λ-$(BETS)_2GaCl_4$ proved by ^{13}C-NMR **25**

6 Introduction 25

7 Motivation 27

8 Experiments 27

9 Results and Discussion 29
- 9.1 NMR shift at ambient pressure 29

9.2 NMR shift under pressure . . . 30
9.3 Spin-lattice relaxation time T_1 . . . 31
9.4 $1/T_1T$ at high-temperature region (above T^*) . . . 32
9.5 $1/T_1T$ at low-temperature region (below T^*) . . . 33
9.6 Korringa factor . . . 34
9.7 Comparison with other organic conductors . . . 35

10 Summary for Part. II 40

III Coupling of molecular motion and electronic state of organic molecular dimer Mott insulator β'-$(ET)_2ICl_2$ proved by ^{1}H- and ^{13}C-NMR 40

11 Introduction 40
11.1 Crystal structure and P-T phase diagram of β'-$(ET)_2ICl_2$ . . . 41
11.2 Dimer Mott insulator . . . 41
11.3 Dimer Mott insulating phase of β'-$(ET)_2ICl_2$ . . . 43
11.4 Charge degrees of freedom in a dimer Mott insulating phase . . . 45
11.5 Dielectric Properties of β'-$(ET)_2ICl_2$ . . . 46
11.6 Field-induced CD state of β'-$(ET)_2ICl_2$ . . . 46

12 Motivation 50
12.1 Background . . . 50
12.2 Ethylene motion . . . 50
12.3 Ethylene motion in κ-type salts . . . 50
12.4 The possible scenario of the charge degrees of freedom due to the ethylene motion . . . 51
12.5 Purpose of our study . . . 52

13 Experiments 52
13.1 Ethylene motion and ^{1}H-NMR study . . . 52
13.1.1 Anomaly in the spin-lattice relaxation time . . . 52
13.1.2 Bloembergen-Purcell-Pound (BPP) theory . . . 53
13.1.3 Ethylene motion and the BPP model . . . 54
13.2 Sample preparation and experimental condition . . . 54
13.2.1 Sample preparation . . . 54
13.2.2 Conditions for ^{1}H-NMR . . . 54

13.2.3 Conditions for ^{13}C-NMR 55

14 Results and Discussion 55
14.1 ^{1}H NMR measurement 55
14.2 ^{13}C-NMR measurement 58
14.3 Coupling mechanism between the ethylene motion and ^{13}C nuclei 59
14.4 The possible origin of the electric dipole in a dimer 61
14.5 Ethylene motion and the dielectric anomaly in β'-$(ET)_2ICl_2$ 63

15 Summary for Part. III 64

References 65

Part I

Pressure effect on electric and magnetic properties in λ-$(ET)_2GaCl_4$ proved by ^{13}C-NMR

1 Introduction

1.1 General characteristics of ET-based organic conductors

BEDT-TTF-based [BEDT-TTF (ET): bis(ethylenedithio)tetrathiafulvalene] crystals, which have ET or similar donor molecules such as us-STF and BETS, and a variety of anion molecules such as I_3^-, ICl_2^-, $Cu(CNS)_2^-$, $RbZn(SCN)_4^-$, consist an important group of organic conductors, where us-STF and BETS denote unsymmetrical-bis(ethylendithio)diselenadithiafulvalen and bis(ethylenedithio)tetraselenafulvalene, respectively. As shown in Fig. 1, they form a layered structure consisting of donor (D) [D = ET, us-STF, BETS (Fig. 2)] layers and the anion layers. In the crystals, two donor molecules provide one electron to one anion molecule on average, that is, a donor molecule works as a donor of electron with the formal charge is +0.5, and an anion works as an acceptor. π electrons on donor molecules form a conduction band due to their relatively large inter-molecular transfer integral. In addition, the Fermi surface is formed due to the hole-doped donor molecules. This gives rise to a conductivity for the donor layer. Hence, the ET-based organic crystal is widely known as a charge transfer complex. The anion layer works as an insulating layer and anion molecules do not contribute to the electric conductivity. This result in the low-dimensional transport property of ET-based crystals.

Donor molecules can take a variety of donor arrangements in a conduction layer as shown in Fig. 3, which is denoted by a Greece letter in front of a compound' s name such as α-, θ-, κ-, λ-type, and so on. Depending on the donor arrangements, ET salts form anisotropic inter-molecular transfer integral. This gives rise to a variety of physical phenomena and various phase diagrams for ET crystals. For example, α- and θ-type salts are usually regarded as quarter-filled systems [1], where there is one charge per two sites as shown in Fig. 4. In this system, the charge-ordered state can be realized due to the on-site and off-site Coulomb repulsions (U) and (V) [2]. Contrary, κ- and λ-type salts form ET dimers in the crystal. In these salts, there is one charge per one dimer unit, hence, the electronic system is regarded as an effective half-filled system (see Fig. 5). In the half-filled system, the charge is localized on a dimer when U is

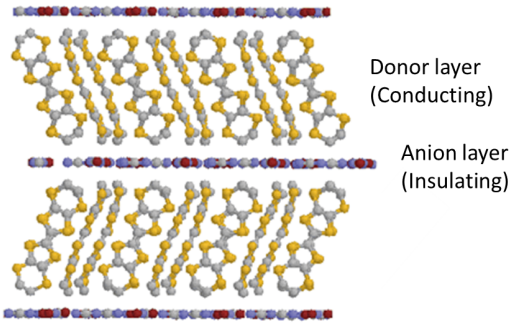

Figure 1: The layered structure of ET-based crystals.

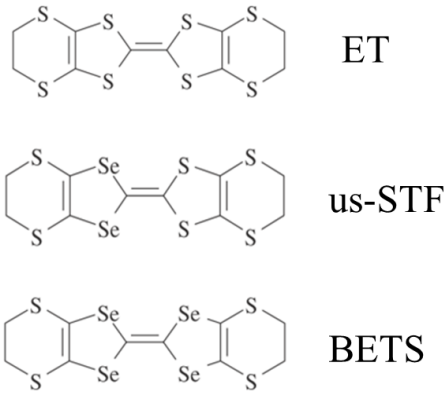

Figure 2: The variation of donor molecules.

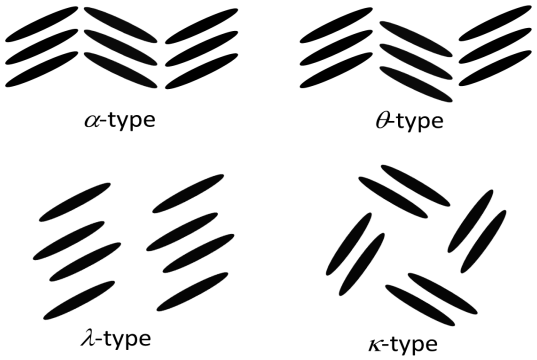

Figure 3: Various donor arrangements in BEDT-TTF salts.

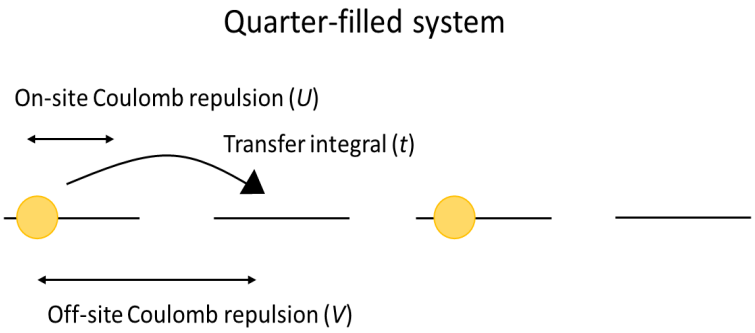

Figure 4: The schematic of the quarter-filled system.

larger than the interdimer transfer integral t, which is known as a Mott transition. Once the Mott transition occurs, the electronic system becomes insulating, namely a dimer Mott insulating phase is realized. In terms of the magnetism, dimer Mott insulator has a localized spin on the dimer. Therefore, a dimer Mott insulator often shows the antiferromagnetic (AF) transition at low temperature due to the AF interaction among the spins [3].

In addition, the difference of the donor arrangement gives rise to the anisotropy of the transport and magnetic properties. This anisotropy of the transport and the magnetic properties and the low-dimensional Fermi surface, curious phase transitions or electronic phase are observed such as spin-Peierls transition, spin density wave (SDW), charge density wave (CDW), and so on. These are unique for low-dimensional conductors. Another advantageous point of organic molecular conductors is that it is easy to control the electronic state by applying pressure because of the soft lattice system. In this

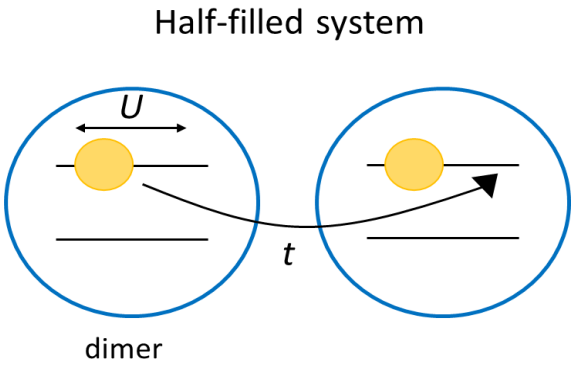

Figure 5: The schematic of the half-filled system.

way, the organic molecular conductors are good candidates to investigate the nature of electronic and magnetic property of a solid-state material.

1.2 Role of organic conductors

Research on organic conductors has significantly contributed to the elucidation of strongly correlated electron systems as well as their unconventional superconductivity. Theoretical and experimental researches have been suggested that the antiferromagnetic (AF) spin fluctuation may contribute to the emergence of superconductivity in the famous ET-based organic conductor κ-$(ET)_2X$ [X: monovalent anion] as well as high-T_c cuprates and some heavy-fermion systems [4–7]. In κ-type organic conductors, the ground state of the insulating phase near the superconducting (SC) phase is the AF insulating phase as shown in Fig. 6 [8]. Indeed, ^{13}C-NMR measurement under pressure for κ-$(ET)_2Cu(NCS)_2$ revealed that Korringa factor is larger than unity, suggesting the existence of strong AF spin correlation (Fig. 7). Moreover, the pressure dependence of Korringa factor is well correlated to the superconducting transition temperature T_c [9]. These results experimentally demonstrated that AF spin interactions are likely to contribute the emergence of superconductivity. Thus, investigation of the relationship between superconductivity and the magnetic properties driven by the adjacent insulating phase is important for exploring the mechanism of unconventional superconductivity.

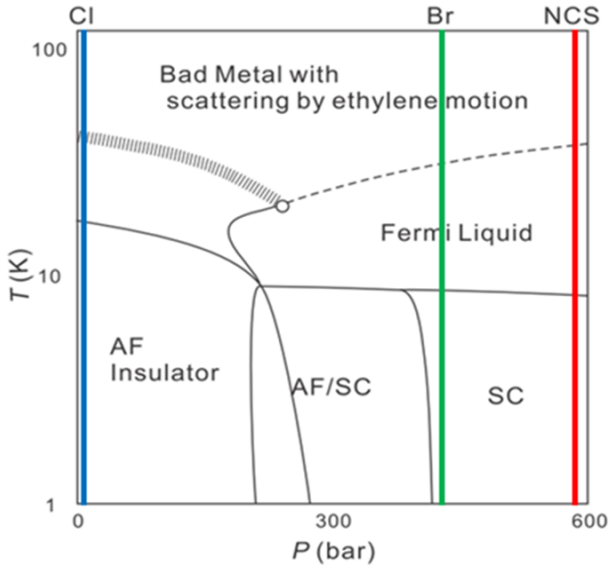

Figure 6: Pressure–temperature phase diagram of κ-$(ET)_2X$ salts.

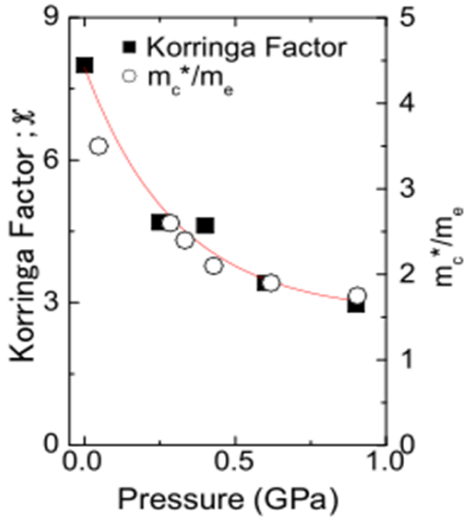

Figure 7: Pressure dependence of Korringa factor of κ-$(ET)_2Cu(NCS)_2$ [9].

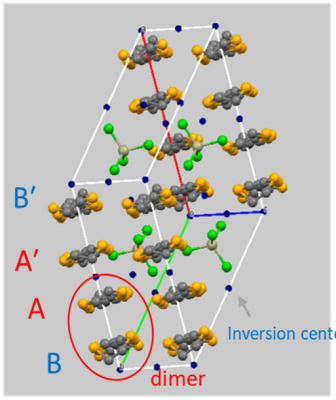

D	ET	STF	BETS
Space group	$P\bar{1}$	$P\bar{1}$	$P\bar{1}$
a [Å]	16.246	16.203	16.172
b [Å]	18.027	18.316	18.616
c [Å]	6.533	6.573	6.607
α [degree]	98.20	98.41	98.38
β [degree]	97.48	97.03	96.75
γ [degree]	112.29	112.42	112.56
V [Å^3]	1716	1750	1784

Figure 8: Crystal structure and lattice parameters of λ-$(D)_2GaCl_4$.

1.3 λ-$(D)_2GaCl_4$ [D = ET, STF, BETS]

Figure 8 shows the crystal structure of λ-$(D)_2GaCl_4$. There two crystallographically independent donor molecules in a unit cell. The space group is $P\bar{1}$, and the inversion symmetry exists. Each independent molecule forms a dimer since the intradimer transfer integral is the largest. The pressure–temperature (P–T) phase diagram of λ-$(D)_2GaCl_4$ [D = ET, us-STF, BETS] has been studied by substituting the donor molecule (Fig. 9) [10–12]. The substitution of inner chalcogen atoms of the donor molecule from sulfur to selenium efficiently increases the transfer integral, inducing an itineracy in an electron system. Hence, λ-$(BETS)_2GaCl_4$ locates at higher pressure region, and λ-$(ET)_2GaCl_4$ is at opposite side. The resistivity measurements revealed that the effect of donor molecule substitution can be regarded as the same as that of physical pressure (Fig. 10) [11]. This enables systematic study of P–T phase diagram of λ-$(D)_2GaCl_4$.

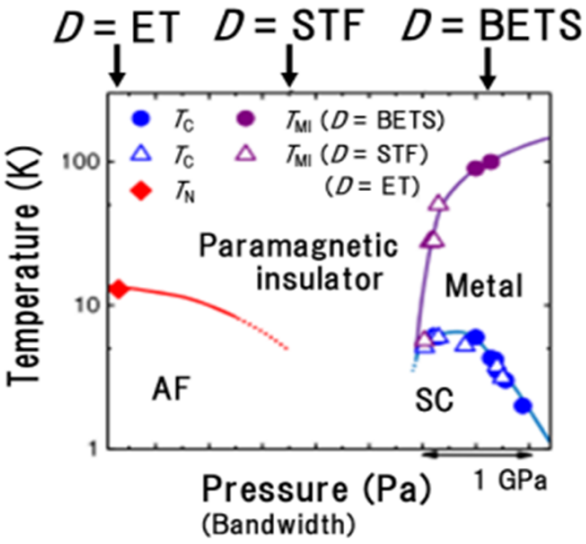

Figure 9: Pressure–temperature phase diagram of λ-$(D)_2GaCl_4$.

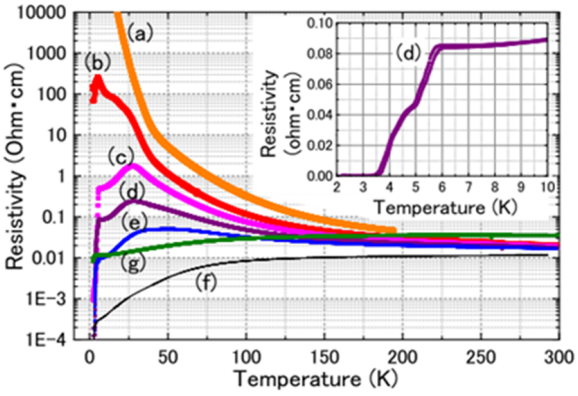

Figure 10: Temperature dependence of the resitivities of λ-$(STF)_2GaCl_4$ at various pressures: (a) 1.10, (b) 1.31, (c) 1.27, (d) 1.31, (e) 1.35, (f) 1.60, and (g) 1.90 GPa. Curves from (a) to (f) were obtained for sample A, and (g) was obtained for sample B. The inset shows the low-temperature region below 10 K at 1.31 GPa. [11].

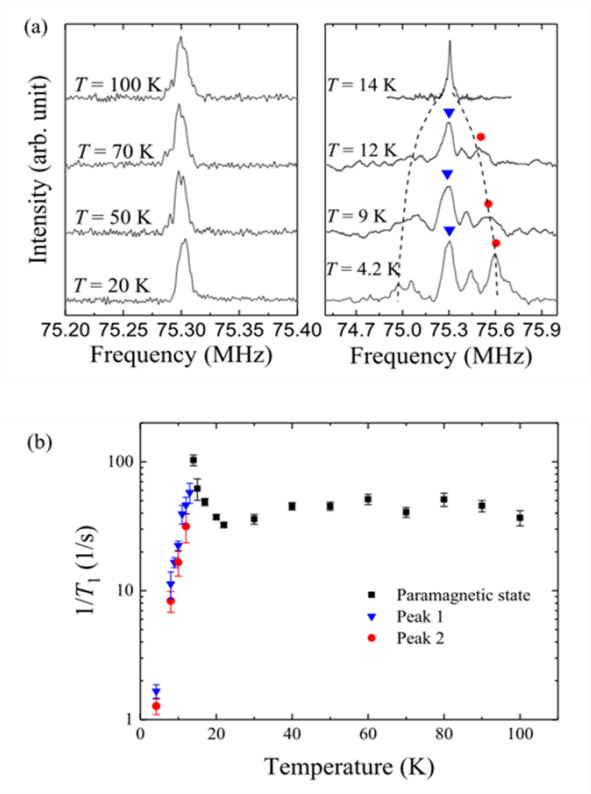

Figure 11: Temperature dependence of (a) the NMR spectra and (b) the nuclear spin-lattice relaxation rate ($1/T_1$) of λ-$(ET)_2GaCl_4$ [13].

1.4 Physical properties of λ-$(ET)_2GaCl_4$

λ-$(ET)_2GaCl_4$ salt locates at lower pressure region in the P–T phase diagram and its electronic property is known as a typical dimer Mott insulator. Indeed, this salt exhibits the insulating behavior from room temperature. Previously, ^{13}C-NMR measurements were conducted at ambient pressure [13]. The NMR spectra split and the nuclear spin-lattice relaxation rate ($1/T_1$) has a peak at 13 K (Fig. 11). This indicates that the antiferromagnetic transition occurs at $T_N = 13$ K.

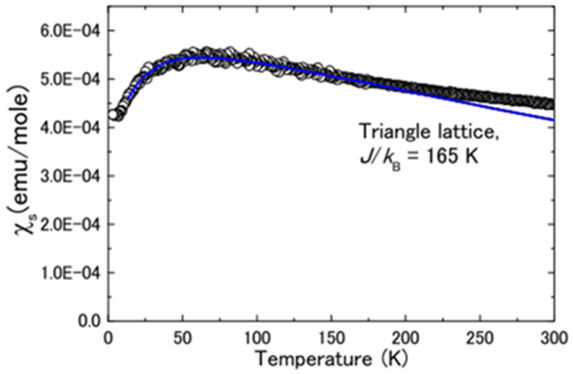

Figure 12: Temperature dependence of the magnetic susceptibility of λ-$(STF)_2GaCl_4$. The Curie-Weiss component was subtracted from the original data [11].

1.5 Physical properties of λ-$(STF)_2GaCl_4$

λ-$(STF)_2GaCl_4$ locates at higher pressure region compared to λ-$(ET)_2GaCl_4$. Previous ^{13}C-NMR study revealed that λ-$(STF)_2GaCl_4$ shows no magnetic ordered state down to 1.6 K despite its relatively strong AF interaction $J/k_B = 165$ K estimated by the temperature dependence of spin susceptibility (see Fig. 12) [11]. Figure 13 shows the temperature dependence of the NMR spectra and $1/T_1T$. No splitting is observed in the NMR spectra, and $1/T_1T$ increases with decreasing temperature down to 1.6 K. Therefore, it is not clear what the magnetic or electrical characteristics of the insulating phase adjacent to the SC phase of BETS salt have.

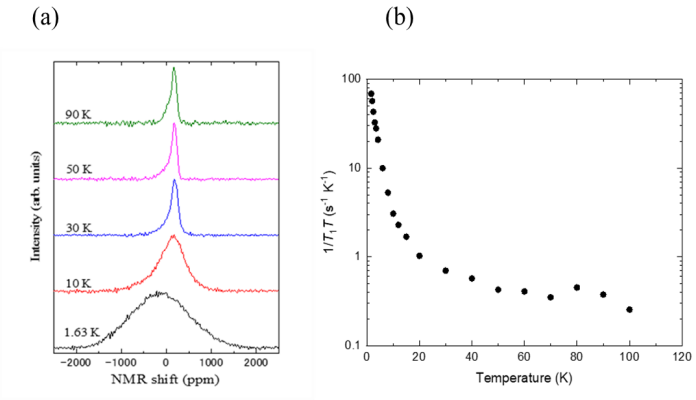

Figure 13: Temperature dependence of (a) NMR spectra and the nuclear spin-lattice relaxation rate divided by temperature ($1/T_1T$) of λ-$(STF)_2GaCl_4$ [measured by Y. Saito].

2 Motivation

Considering the low-pressure region of the P–T phase diagram of λ-$(D)_2GaCl_4$, there are a few questions that how the AF phase behaves under pressure and whether the absence of magnetic order in the STF region is intrinsic. Indeed, it has been pointed out that the absence of magnetic ordering in λ-$(STF)_2GaCl_4$ can be attributed to the disorders in the donor layer. In the STF molecule, there is an asymmetry that originates from the difference in electron orbital radii between sulfur and selenium atoms beside the central C=C bond (Fig. 14). This asymmetry may modulate the magnitude of AF interaction between donor molecules and give rise to the effect of disorder. This can interfere with magnetic order. Hence, we investigated the electric and magnetic properties in λ-$(ET)_2GaCl_4$ under pressure via ^{13}C-NMR since the ET molecule is symmetric donor. In this part, we focus on the behavior of the AF phase under pressure and discuss whether the absence of magnetic order in the STF region is intrinsic.

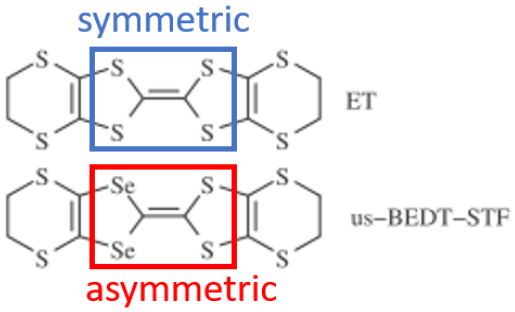

Figure 14: Schematic of ET and STF molecules.

3 Experiments

3.1 Sample preparation and settings

Single crystal of λ-$(ET)_2GaCl_4$ were synthesized by the standard electrochemical method. The one side of central C=C bond of BETS molecule was enriched by ^{13}C to avoid Pake doublet problem (Fig. 16) [14]. The central carbons are suitable site for measuring ^{13}C NMR because the electron density of the highest occupied molecular orbital (HOMO) is the largest around the central C=C bond, which enables us to investigate the electronic state sensitively. Typical size of the sample used in NMR measurement is $2.4 \times 0.2 \times 0.1$ mm^3. We used NiCrAl cramp cell for pressurizing and Daphne 7474 oil as a pressure medium (see Fig. 17). The applied pressures were 4, 10 and 20 kbar, which were calibrated at low temperature.

3.2 Sample identification

For sample identification, we measured the temperature dependence of NMR spectra and the value of T_1 at 80 K at ambient pressure for λ-$(ET)_2GaCl_4$. We confirmed that the value of T_1 is almost 10 ms, which is comparable to that in previous study [13]. In addition, NMR spectral intensity was dramatically changed at around 13 K as shown in Fig. 15, indicating the AF transition. Hence, the sample was confirmed to be λ-type.

3.3 Condition of NMR measurement

The NMR measurement was conducted with a magnetic field of 6.0 T. The magnetic field was applied in the direction of (110) (see Fig. 18(a)). The NMR spectra were

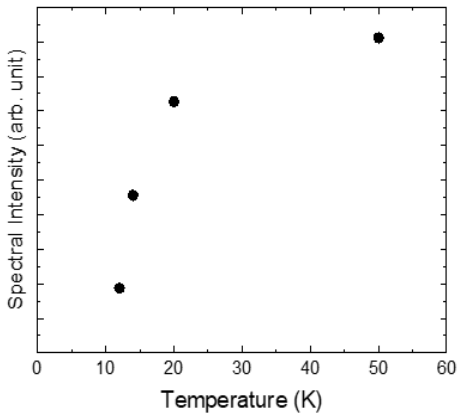

Figure 15: NMR spectral intensity at various temperatures.

Figure 16: Schematic of ^{13}C enriched ET molecule.

obtained by fast Fourier transformation of the echo signal with $\pi/2$–π pulse sequence. The typical value of $\pi/2$ pulse length were 1.5 μs. The NMR shifts were measured with respect to the reference material of tetramethylsilane (TMS). The spin-lattice relaxation times (T_1) were measured by the conventional saturation-recovery method.

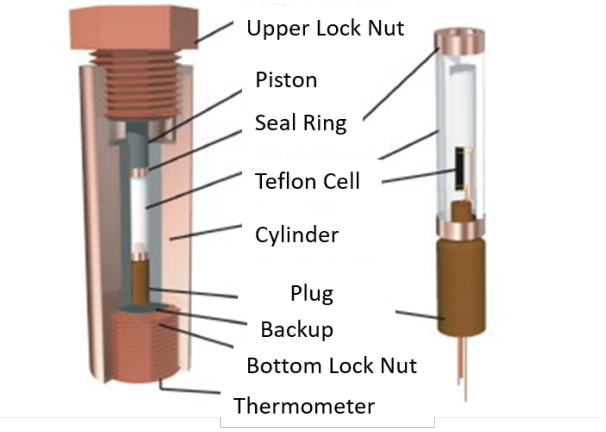

Figure 17: Schematic of NiCrAl cramp cell.

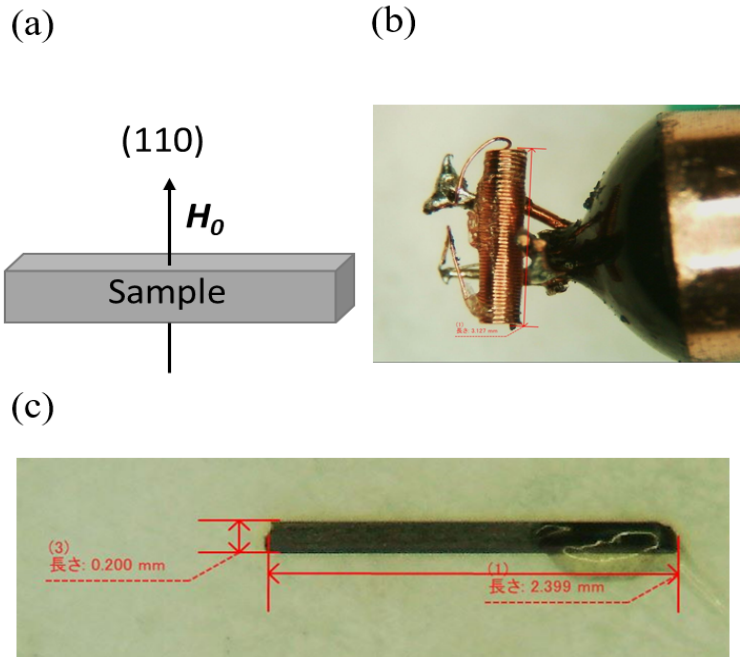

Figure 18: (a) The direction of applied magnetic field. (b) NMR coil set in the pressure cell plug. The length of NMR coil is about 3 mm. (c) The single crystal of λ-type salt. The typical size is $2.4 \times 0.2 \times 0.05$ mm^3.

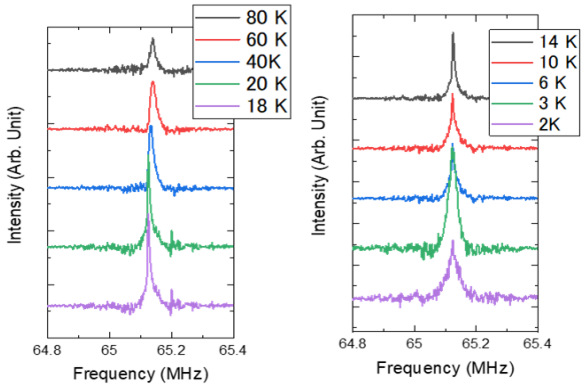

Figure 19: NMR spectra of λ-$(ET)_2GaCl_4$ at 4 kbar.

4 Results and Discussion

4.1 NMR spectra and $1/T_1T$

Figure 19 shows the temperature dependence of ^{13}C-NMR spectra of λ-$(ET)_2GaCl_4$ at 4 kbar. One peak is observed from 80 K down to 2 K. Figure 20 shows the temperature dependence of $1/T_1T$ at ambient pressure and 4 kbar. The data for ambient pressure is the reference of previous ^{13}C-NMR study. At 4 kbar, $1/T_1T$ has a peak at 3 K. Generally, $1/T_1T$ is written by following equation,

$$\frac{1}{T_1T} = \frac{2\gamma_n^2 k_B}{(\gamma_e\hbar)^2}\sum_q A_\perp^2(q)\frac{\chi''_\perp(q)}{\omega}, \tag{1}$$

where, $A_\perp(q)$ and ω are the hyperfine coupling constants perpendicular to the field direction and the NMR frequency, respectively. $\chi''_\perp(q)$ represents the imaginary part of dynamic spin susceptibility perpendicular to the field direction with wave vector q. $1/T_1T$ increases when the electron system has a spin fluctuation, and has a peak when a magnetic transition occurs. Since λ-$(ET)_2GaCl_4$ shows the AF transition at 13 K at ambient pressure, this peak structure indicates the AF transition. Moreover, the AF transition is easily suppressed by applying pressure. At 10 and 20 kbar, $1/T_1T$ does not show the peak structure, instead, continues to increase with decreasing temperature down to 3 K. This result indicates that the AF transition is suppressed at least down to 3 K under 10 and 20 kbar. The pressure of 20 kbar for λ-$(ET)_2GaCl_4$ is almost comparable to the location of λ-$(STF)_2GaCl_4$ in the P–T phase diagram, hence, this result indicates the absence of magnetic order in λ-$(ET)_2GaCl_4$. This means that

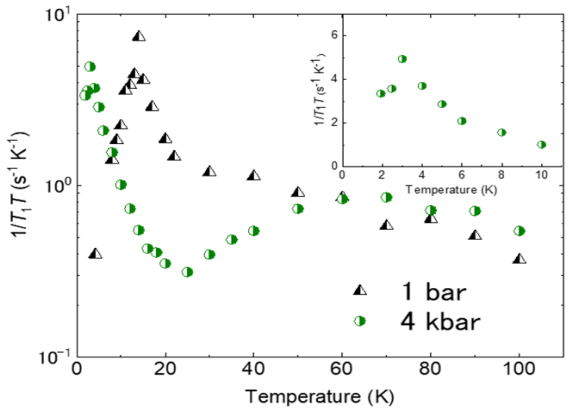

Figure 20: $1/T_1T$ of λ-$(ET)_2GaCl_4$ at ambient pressure and 4 kbar.

asymmetry in the donor molecule has a little effect on the absence of magnetic order in λ-$(STF)_2GaCl_4$, rather, that is intrinsic for the electronic property of λ-type organic conductors (Fig. 22).

4.2 NMR shift

Figure 23 shows the temperature dependence of NMR shift (raw data) under each pressure. At ambient pressure and 4 kbar, the NMR shift shows almost same behavior, however, its behavior is dramatically changed at 10 and 20 kbar especially in high temperature region. In fact, the heater wire was broken and rewound when applying a pressure of 10 kbar. At that time, it seems that an extra magnetic field was applied while the heater was being struck because the non-inductive winding was not performed. Therefore, the reliability of the data was poor and it was necessary to perform remeasurement.

4.3 Difficulty in λ-$(ET)_2GaCl_4$

We tried to synthesize the crystal of λ-$(ET)_2GaCl_4$ for the remeasurement. However, it was revealed by X-ray structural analysis that most of the samples were not λ-type but another crystal system called δ-type (Fig. 24). The physical property of δ-type salt is quite different from that of λ-type; hence, it is not suitable for this measurement. In the combination of ET and $GaCl_4$, λ-type crystal is minor products, and it was difficult to obtain a sample of a size suitable for NMR. Therefore, the remeasurement is currently

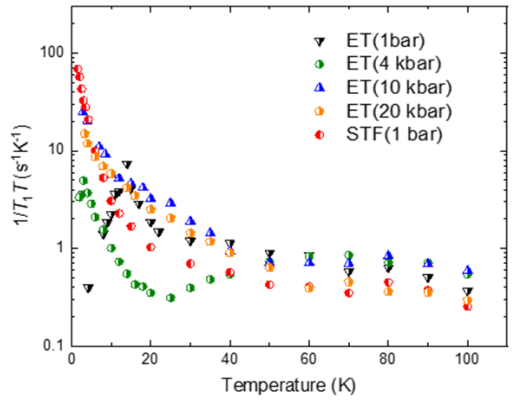

Figure 21: $1/T_1T$ of λ-$(ET)_2GaCl_4$ at 1 bar [13] and 4, 10 and 20 kbar. As a reference, the previous result of λ-$(STF)_2GaCl_4$ is plotted [measured by Y. Saito et al.].

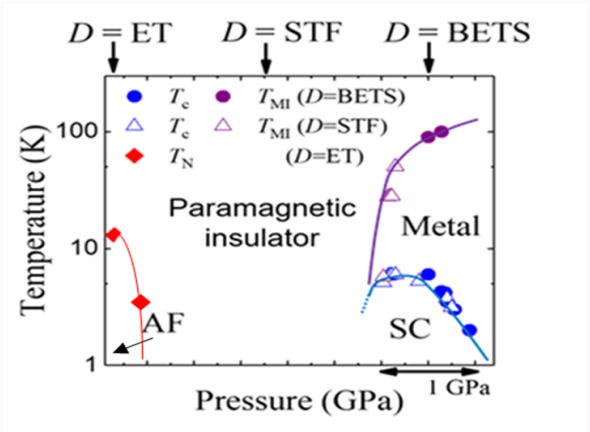

Figure 22: The updated P–T phase diagram of λ-$(D)_2GaCl_4$.

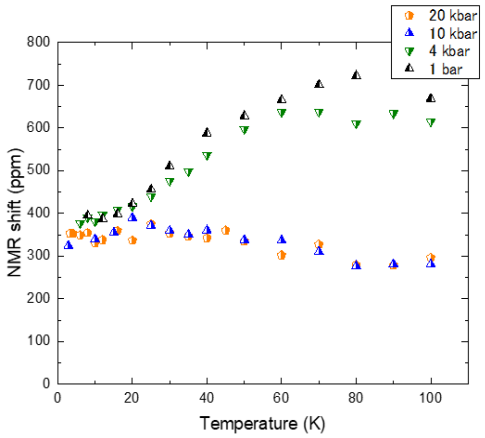

Figure 23: Temperature dependence of NMR shift at each pressures.

suspended.

4.4 Alternate options

Recently, a single crystal of λ-$(BEST)_2GaCl_4$ [BEST: bis(ethylenedithio)diselenadithiafulvalene] was synthesized, and it is known that λ-$(BEST)_2GaCl_4$is located on the negative pressure side of the λ-$(ET)_2GaCl_4$ in the P–T phase diagram. Furthermore, the AF transition was confirmed around 21 K, suggesting the connection of electronic properties with the ET salt by applying pressure (Fig. 25). Figure 26 shows the muon spin rotation (μSR) time spectra in λ-$(ET)_2GaCl_4$ and λ-$(BEST)_2GaCl_4$. In λ-$(ET)_2GaCl_4$, the time spectra indicate that the internal field is inhomogeneous. In contrast, the time spectra in λ-$(BEST)_2GaCl_4$ indicates multiple homogeneous internal fields, suggesting the simple up-down AF structure. This property is convenient for exploring the behavior of AF in the P–T phase diagram. In addition, λ-$(BEST)_2GaCl_4$ is easier to synthesize than λ-$(ET)_2GaCl_4$, and there is no by-products. Hence, it is more suitable for studying the behavior of the AF phase to investigate the electronic and magnetic properties of λ-$(BEST)_2GaCl_4$ under pressure. Currently, ^{13}C-NMR under pressure for λ-$(BEST)_2GaCl_4$ is planned, and it is expected that new findings will be obtained.

Table 1. Crystallographic Data for $(BEDT\text{-}TTF)_2GaCl_4$

$C_{20}H_{16}S_{16}GaCl_4$	fw = 980.9
$a = 31.911(6)$ Å	space group = $P\bar{1}$ (No. 2)
$b = 16.580(4)$ Å	$T = 298$ K
$c = 6.645(2)$ Å	$\lambda = 1.5418$ Å
$\alpha = 98.15(2)°$	$\rho_{calcd} = 1.878$ g cm^{-3}
$\beta = 85.60(2)°$	$\mu = 127.23$ cm^{-1}
$\gamma = 90.55(2)°$	$R = 4.7\%^a$
$V = 3470$ Å^3	$R_w = 4.8\%^a$
$Z = 4$	

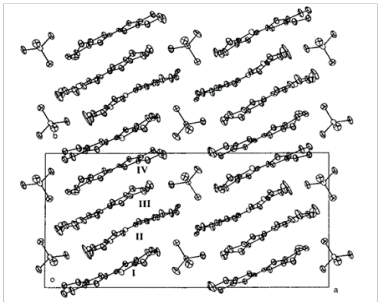

Figure 24: Cell parameter and crystal structure of δ-$(ET)_2GaCl_4$.

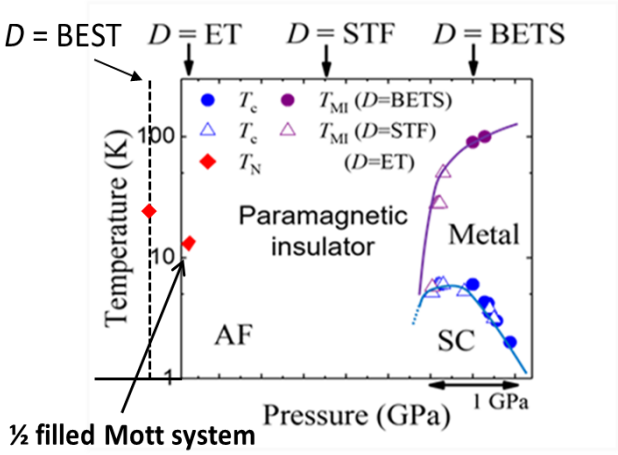

Figure 25: P–T phase diagram of λ-$(D)_2GaCl_4$ with λ-$(BEST)_2GaCl_4$.

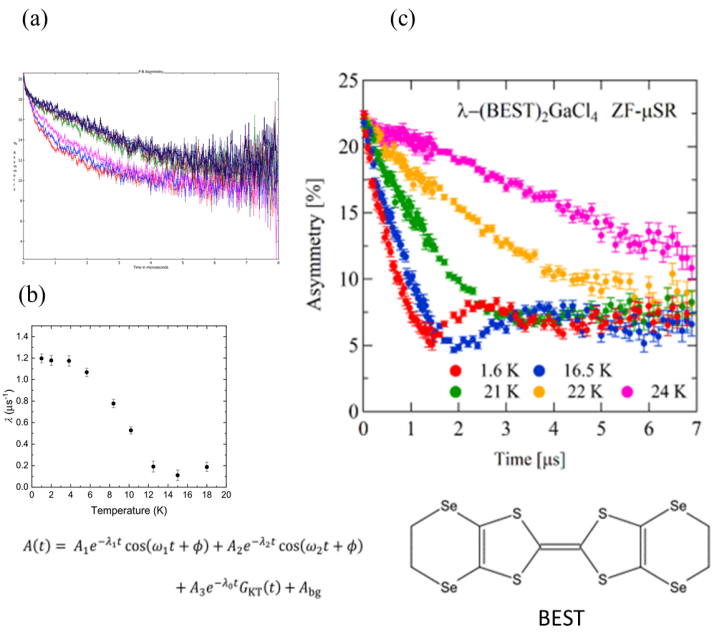

Figure 26: (a) μSR time spectra in λ-$(ET)_2GaCl_4$ (raw data). (b) Temperature dependence of the precession frequency in λ-$(ET)_2GaCl_4$. (c) ZF-μSR time spectra in λ-$(BEST)_2GaCl_4$.

5 Summary for Part. I

For summarize, we performed ^{13}C-NMR in λ-$(ET)_2GaCl_4$ under pressure to investigate the behavior of the AF phase. We revealed that the AF transition temperature decreases at 4 kbar ($T_N = 3$ K), and the AF transition is suppressed ($T_N \leq 3$ K) at 10 and 20 kbar. This result indicates that the AF phase in λ-$(ET)_2GaCl_4$ is quickly suppressed by applying pressure and the absence of magnetic order in λ-$(STF)_2GaCl_4$ seems to be intrinsic, which means that the effect of disorder in the donor layer does not contribute to magnetism. The results of our NMR shifts require remeasurement as the reliability of the data is compromised by experimental mistakes. However, the experiment was suspended due to the difficulties in synthesizing a sample. Instead, it is considered to be a useful option to investigate the electronic and magnetic properties under pressure in λ-$(BEST)_2GaCl_4$, which shows a simple AF structure and is easy to synthesize.

Part II

Enhancement of electron correlation and SDW fluctuations under pressure of λ-$(BETS)_2GaCl_4$ proved by ^{13}C-NMR

6 Introduction

Quasi-two-dimensional organic conductor λ-$(BETS)_2GaCl_4$ is a paramagnetic metal and shows SC transition at 6 K at ambient pressure [15]. This compound has attracted much attention because d-wave SC gap function has been reported by the thermodynamic study [16]. In addition, the possibility of Fulde–Ferrell–Larkin–Ovchinnikov state near the upper critical field has been suggested by several experiments [17–19]. In the isomorphic compound λ-$(BETS)_2FeCl_4$, the interaction between π-electron of BETS molecule and d-electron of Fe ions (π–d interaction) plays a crucial role to determine the electronic and magnetic properties. In this salt, AF transition with metal-insulator (M-I) transition occurs at 8 K instead of SC transition [20]. Moreover, this salt exhibits the field-induced superconductivity under high magnetic field of 17 T [21]. These phenomena have attracted much interest; therefore, λ-type organic conductors have been actively researched.

The phase diagram of λ-$(BETS)_2GaCl_4$ has also been investigated in alloy system λ-$(BETS)_2GaBr_xCl_{4-x}$ ($0 \leq x \leq 2$) (Fig. 27) [12]. With increasing x, the cell volume increases, and the effective transfer integral is decreased. As a result, the insulating phase is induced in the larger x region. The resistivity measurement revealed that the sample with $x = 0.75$ shows M-I transition around 13 K [22]. Recent ^{13}C-NMR studies have revealed the existence of commensurate SDW ordered phase below 13 K [23], predicting that the phase adjacent to SC phase of λ-$(BETS)_2GaCl_4$ is SDW ordered phase. Actually, ^{13}C-NMR measurement for λ-$(BETS)_2GaCl_4$ at ambient pressure have revealed that the spin-lattice relaxation rate divided by temperature ($1/T_1T$) increases below 10 K towards the lowest temperature, indicating the existence of SDW fluctuation even in the sample with $x = 0.0$ (Fig. 28) [24].

Considering above, it is important to investigate the relationship between SDW fluctuation and the superconductivity in λ-$(BETS)_2GaCl_4$. $(TMTSF)_2PF_6$ is famous organic conductor in which the SDW phase is adjacent to the SC phase [25]. ^{13}C-NMR measurement under pressure has revealed that $1/T_1T$ is significantly increased at low

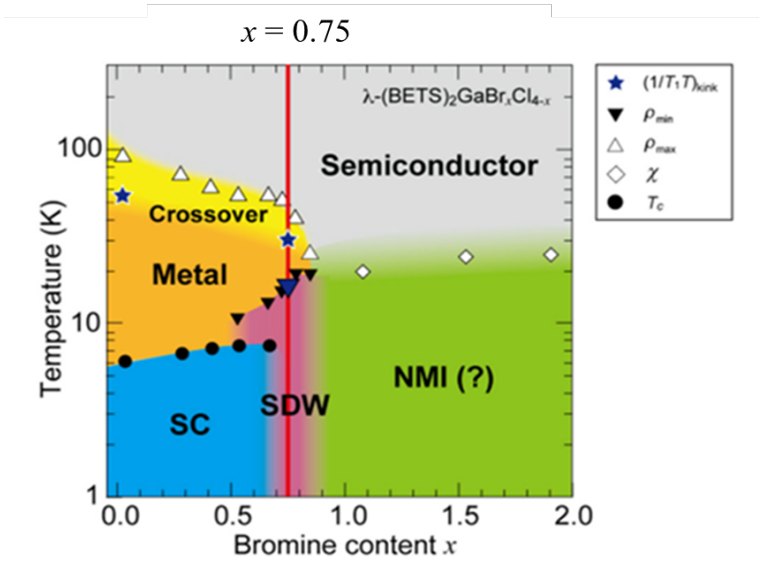

Figure 27: Phase diagram of λ-$(BETS)_2GaBr_xCl_{4-x}$ with bromine content x.

temperature, indicating the SDW fluctuation [26]. In addition, pressure dependence of the enhancement of $1/T_1T$ is correlated well with that of T_c, implying essential relevance between SDW fluctuation and the emergence of superconductivity.

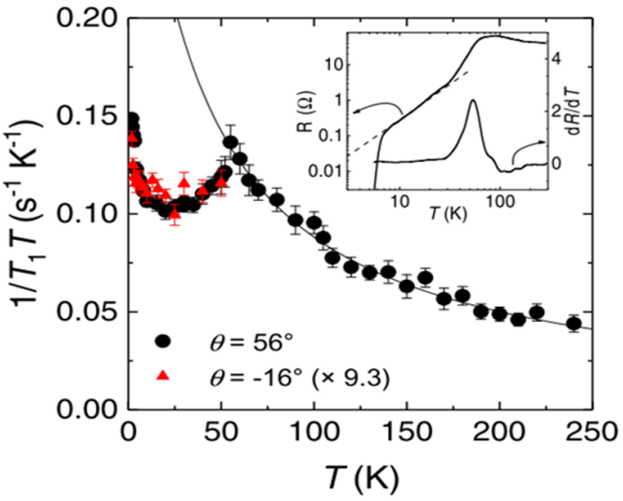

Figure 28: Temperature dependence of $1/T_1T$ of λ-$(BETS)_2GaCl_4$ measured by ^{13}C-NMR at ambient pressure [24].

7 Motivation

In λ-$(BETS)_2GaCl_4$, the SDW fluctuation at low temperature has been investigated only at ambient pressure. Hence, it is desirable to investigate the pressure dependence of SDW fluctuation for revealing the relationship between SDW fluctuation and superconductivity. In this paper, we report the result of ^{13}C-NMR measurement under pressure for λ-$(BETS)_2GaCl_4$. In this salt, T_c is suppressed when the pressure is applied and completely disappears at the certain pressure or higher [12], and the electronic system becomes Fermi liquid state. Therefore, we focus on the pressure effect on SDW fluctuations and discuss qualitatively the relationship between SDW fluctuations and T_c.

8 Experiments

Single crystasl of λ-$(BETS)_2GaCl_4$ were systhesized by the standard electrochemical method [27]. Figure 29(a) shows the crystal structure of λ-$(BETS)_2GaCl_4$. The one side of central C=C bond of BETS molecule was enriched by ^{13}C to avoid Pake doublet problem (Fig. 29(b)) [14]. The central carbons are suitable site for measuring ^{13}C-NMR because the electron density of the highest occupied molecular orbital (HOMO) is the largest around the central C=C bond, which enables us to investigate the electronic state sensitively. Typical size of the sample used in NMR measurement is $2.4\times0.2\times0.05$ mm^3.

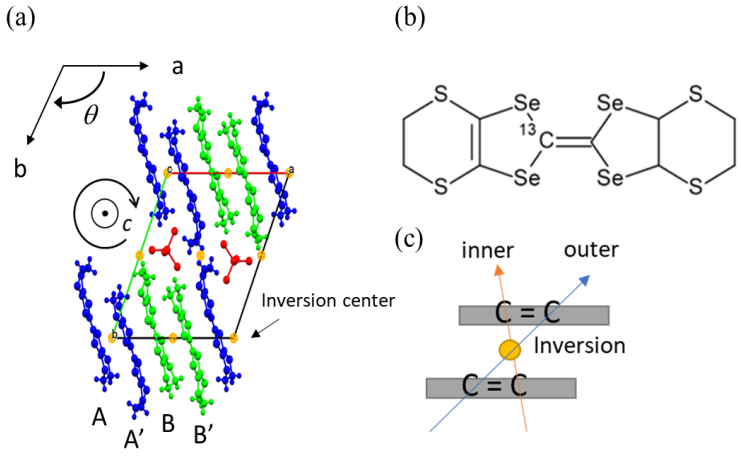

Figure 29: (a) Crystal structure of λ-$(BETS)_2GaCl_4$. The green and blue molecules represent crystallographically independent molecule. Yellow dots represent the inversion symmetry. (b) ^{13}C enriched BETS molecule. (c) Crystallographically independent ^{13}C cites (inner and outer cite).

We used NiCrAl cramp cell for pressurizing and Daphne 7474 oil as a pressure medium. The applied pressures were 3, 6 and 11 kbar, which were calibrated at low temperature. The NMR measurement was conducted with a magnetic field of 6.0 T. The magnetic field was applied in the direction in which the hyperfine coupling constant was the smallest, that is, paralell to the long axis of BETS molecule (see Fig. 29(a)). This direction is convenient for our measurement since the value of T_1 becomes the shortest and almost all peaks are superposed [24]. In this field direction, the upper critical field at 1.5 K is substantially lower than 6 T, so that the SC sate is completely suppressed in the present NMR measurement. The NMR spectra were obtained by fast Fourier transformation of the echo signal with $\pi/2$–π pulse sequence. The typical value of $\pi/2$ pulse length were 1.5 μs. The NMR shifts were measured with respect to the reference material of tetramethylsilane (TMS). The spin-lattice relaxation times (T_1) were measured by the conventional saturation-recovery method.

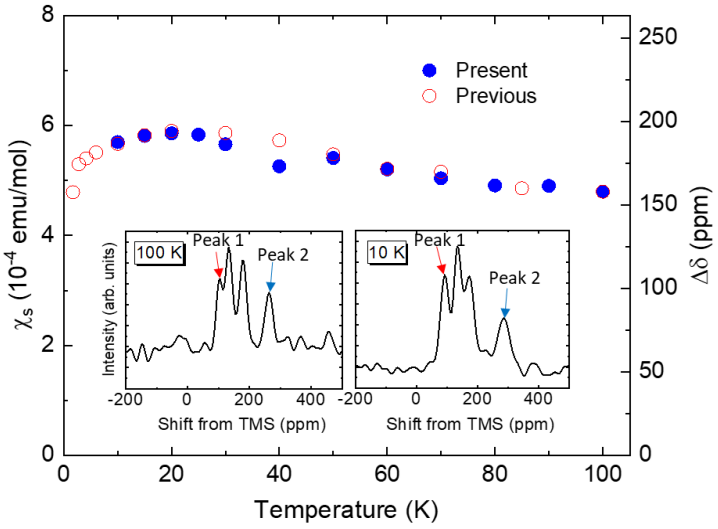

Figure 30: Temperature dependence of the difference of NMR shift (right axis) and spin susceptibility (left axis). The inset shows the NMR spectra at 10 and 100 K. The red and blue arrows show the peak 1 and peak 2.

9 Results and Discussion

9.1 NMR shift at ambient pressure

λ-$(BETS)_2GaCl_4$ salt has two crystallographically non-equivalent molecules A and B, which has equivalent molecule linked by the inversion symmetry A′ and B′, respectively [see Fig. 29(a)]. In addition, there are two crystallographically nonequivalent ^{13}C sites (so-called,"inner" and"outer" sites)[see Fig. 29(c)], so that four peaks can be expected in NMR spectra. The deviation of the resonance frequency from the standard sample (TMS) is called an NMR shift (δ), and it contains various information. In general, the NMR shift is expressed by the sum of the Knight shift (K_s) and the chemical shift (σ); $\delta = K_s + \sigma$. The Knight shift is proportional to the local spin susceptibility of electron (χ_s), that is, $K_s = A_{\rm hf}\chi_s$, where, $A_{\rm hf}$ is a hyperfine coupling constant. We can evaluate χ_s from K_s and $A_{\rm hf}$. Note that σ is unique for a molecule and is usually temperature independent. In addition to these, the magnetism of the pressure cell ($\chi_{\rm cell}$) must also be taken in account. As a total, the NMR shift is written as $\delta = A_{\rm hf}\chi_s + \sigma + B\chi_{\rm cell}$, where, B is a constant. Although we need to estimate $B\chi_{\rm cell}$ and σ experimentally to evaluate χ_s, fortunately, we observed that the four peaks were slightly separated because

of the slightly off-axial field direction. Hence, we utilized the difference of NMR shifts to cancel out the effect of $B\chi_{\rm cell}$ and σ. Note that the $B\chi_{\rm cell}$ and σ can be regarded as the same value for the four peaks [28]. We employed the distant peaks in the spectrum as peak 1 and peak 2, respectively (see the inset of Fig. 30). The NMR shift for peak 1 and peak 2 can be written as following Eq. (2) and Eq. (3).

$$\delta_1 = A_{\rm hf1}\chi_s + \sigma + B\chi_{\rm cell} \tag{2}$$

$$\delta_2 = A_{\rm hf2}\chi_s + \sigma + B\chi_{\rm cell} \tag{3}$$

$$\Delta\delta = \delta_2 - \delta_1 = (A_{\rm hf2} - A_{\rm hf1})\chi_s \tag{4}$$

We can obtain Eq. (4) from the difference Eq. (3) – Eq. (2). The right axis in Fig. 30 represents the temperature dependence of $\Delta\delta$ at ambient pressure which is obtained by utilizing the difference of NMR shifts between peak 1 and 2. The coefficient $A_{\rm hf2} - A_{\rm hf1}$ ($\approx$1.9 kOe/μ_B) was determined so that the value of local spin susceptibility at 100 K was completely consistent with that of previous ^{13}C-NMR study. This enabled us to obtain the temperature dependence of χ_s, since the coefficient $A_{\rm hf2} - A_{\rm hf1}$ is temperature independent. As shown in Fig. 30, our results reproduce well the previous study in the whole temperature range. Moreover, χ_s shows a broad hump structure near 20 K, which is also confirmed by the previous study [24]. These guarantee the validity of our analysis.

9.2 NMR shift under pressure

The temperature dependence of χ_s under pressure was also evaluated in the same manner. Figure 31(a) shows the NMR spectra under each pressure at 50 K. The spectrum at 3 kbar looks broader, which is thought to be due to the strain associated with the pressure application. At 11 kbar, signals from Daphne oil appeared in the spectrum around 80-100 K because of relatively longer T_1 of λ-(BETS)$_2$GaCl$_4$, and this made it difficult to assign the peak 1 and 2. Below 70 K, since the T_1 of the sample became sufficiently shorter than that of the oil, the signal from the oil could be removed. Therefore, we employed only the data below 70 K for 11 kbar. The broad hump structure around 20 K observed at ambient pressure is suppressed by applying pressure, and χ_s exhibits almost temperature independent behavior at 6 and 11 kbar. This indicates that the electronic system exhibits Fermi liquid state over a wider temperature range under pressure. Moreover, the absolute value of χ_s is reduced under pressure. This can be attributed to the reduction of the density of states (DOS) at the Fermi surface since the band width is widened by applying pressure.

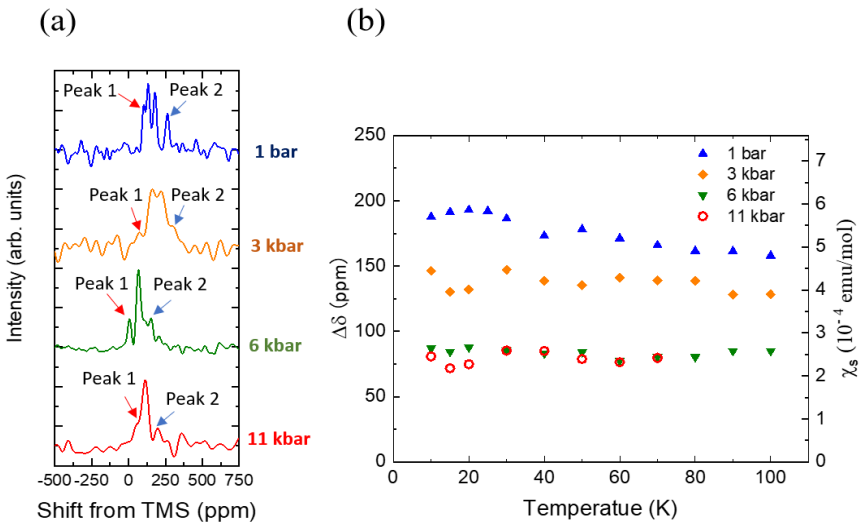

Figure 31: (a) NMR spectra at each pressures at 50 K. The red and blue arrows show peak 1 and peak 2, respectively. (b) Temperature dependence of spin susceptibility at each pressures.

9.3 Spin-lattice relaxation time T_1

The spin-lattice relaxation time T_1 provides significant information on spin fluctuations. In our measurement, T_1 was evaluated from the peak which consists of four ^{13}C sites. Since each ^{13}C site has a slightly different T_1, the recovery profiles deviate from the single exponential function. To correct this deviation, we employed a stretched exponential function, $M(t) = M_0\{1 - \exp(-t/T_1)^\beta\}$. Here, $M(t)$ and M_0 are the nuclear magnetizations at the certain time (t) and at thermal equilibrium, respectively, and β is the stretching exponent. In previous report, β is set as 0.8 in the whole temperature range [24]. To ensure that the recovery profile does not change under pressure, we plotted $\log\{(M_0 - M(t/T_1))/M_0\}$ against t/T_1 as shown in Fig. 32. The solid curve shows the streached exponential function with $\beta = 0.8$. The experimental data were well reproduced by the solid curve even under pressure, indicating that the recovery profile does not change. Figure 33 shows the temperature dependence of $1/T_1T$. The inset shows the result of previous study at ambient pressure [24]. The result at ambient pressure is consistent with the previous one. At ambient pressure, $1/T_1T$ increases as the temperature is lowered and has a peak at 55 K, which is denoted by T^*. T^* can be seen at 70 K under the pressure of 3 kbar. Above 6 kbar, it is difficult to determine T^*

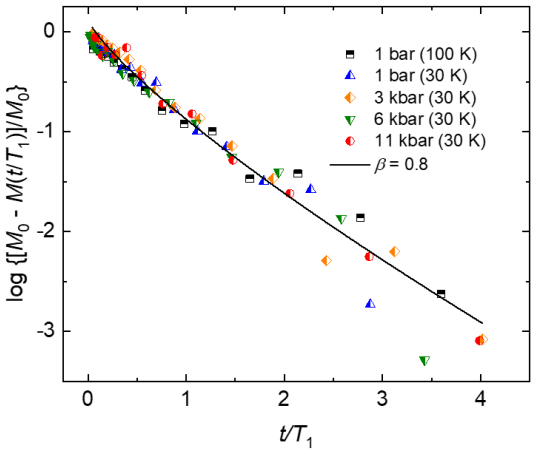

Figure 32: Recovery profiles at each pressures. The solid curve shows the recovery curve with $\beta = 0.8$.

because T^* is thought to be shifted to above 100 K. At 11 kbar, $1/T_1T$ becomes almost constant in the whole temperature range.

9.4 $1/T_1T$ at high-temperature region (above T^*)

In this section, we discuss the behavior of $1/T_1T$ above T^*. Generally, $1/T_1T$ is written as Eq. (1). When the system has a two-dimensional AF spin fluctuation, the temperature dependence of $1/T_1T$ can be described by Curie-Weiss (CW) function, $1/T_1T = C/(T + \Theta)$ as shown in the inset of Fig. 33 [29]. Here, C and Θ correspond to Curie constant and Weiss temperature. In previous study, it has been confirmed that the increase in $1/T_1T$ at high temperature can be attributed to the AF spin fluctuation which derived from the localized electron system, as confirmed in the dimer Mott system of λ-$(ET)_2GaCl_4$ [24]. Our results show that the T^* shifts to higher temperature region by applying pressure. The similar behavior of T^* has also been reported in κ-$(ET)_2Cu(NCS)_2$ [9]. Since the metal-semiconductor crossover occurs at T^*, these results indicate the increase of itenerancy by applying pressure. This is also supported by the reduction of DOS in association with the widenning of bandwidth.

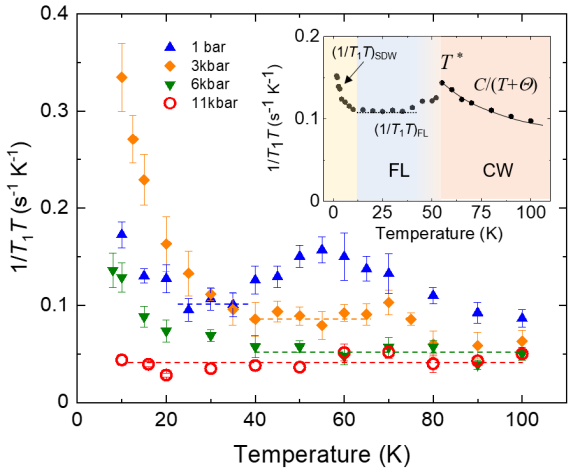

Figure 33: Temperature dependence of $1/T_1T$ at each pressures. The inset shows the result of previous study [24].

9.5 $1/T_1T$ at low-temperature region (below T^*)

In this section, we focus on the behavior of $1/T_1T$ below T^*. At ambient pressure, $1/T_1T$ shows temperature independent behavior below T^* towards around 10 K, indicating the Fermi liquid (FL) state. Below 10 K, $1/T_1T$ turns to increase down to the lowest temperature. This increase in $1/T_1T$ can be attributed to the SDW fluctuation since the SDW ordered phase has been confirmed in λ-$(BETS)_2GaBr_{0.75}Cl_{3.25}$. Therefore, $1/T_1T$ below T^* can be described by the sum of the two terms, that is, a term originats from SDW fluctuations $(1/T_1T)_{SDW}$ and one derived from the itinerant electron system $(1/T_1T)_{FL}$, as follows,

$$\frac{1}{T_1T} = \left(\frac{1}{T_1T}\right)_{SDW} + \left(\frac{1}{T_1T}\right)_{FL}. \tag{5}$$

Here, $(1/T_1T)_{FL}$ was determined by the averaged value of $1/T_1T$ in the FL state as shown by the dotted lines in Fig. 33. This term will be discussed in the next Sec. 9.6. The increase in $1/T_1T$ at low temperatures can be attributed to the SDW fluctuaton. Remarkably, the increase of $1/T_1T$ at 3 kbar is greater than that of ambient pressure, indicating that the SDW fluctuation is enhanced by applying pressure. At 6 kbar, the increase in $1/T_1T$ still remains at low temperature, however, the value of $1/T_1T$ is reduced compared to that of 3 kbar. At 11 kbar, the increase in $1/T_1T$ is mostly suppressed, indicating the disappearing of the SDW fluctuation. The temperature independent behavior of $1/T_1T$ at 11 kbar indicates that the electron system becomes Fermi liquid down

to the lowest temperature.

9.6 Korringa factor

Next, we focus on $(1/T_1T)_{\rm FL}$. $(1/T_1T)_{\rm FL}$ reflects the DOS at the Fermi energy ($N(E_F)$) and has an important information on electron correlation. Since the electronic state is itinerant, $(1/T_1T)_{\rm FL}$ satisfies Korringa relation as follows,

$$\frac{1}{(T_1T)_{\rm FL}K_s^2} = \left(\frac{A_\perp}{\sqrt{2}A_\parallel}\right)^2 \frac{4\pi k_B}{\hbar}\left(\frac{\gamma_n}{\gamma_e}\right)^2 \mathcal{K}, \tag{6}$$

here, K_s is Knight shift and $\mathcal{K}$ is Korringa factor. γ_n and γ_e are the gyromagnetic ratios of nuclear and electron spin, respectively. Usually, Korringa factor characterizes the electron correlation. When an electronic system is normal metal, $\mathcal{K} = 1$ is expected. If an electronic system has antiferromagnetic (ferromagnetic) correlations, $\mathcal{K} > 1$ ($\mathcal{K} < 1$) is expected, respectively. In order to evaluate the form factor $(A_\perp/\sqrt{2}A_\parallel)$, we utilize the hyperfine coupling tensor of κ-$(ET)_2Cu(NCS)_2$ which has the similar dimer structure. Although BETS is Se-analog of ET molecule, the electron density of HOMO at ^{13}C site in BETS is comparable to that in ET. In addition, the overlap mode of a dimer, so called "bond–over–ring", are the same for both κ-type and λ-type [27,30]. Indeed, when a magnetic field is applied in the molecular plane, the NMR shift is almost the same between ET and BETS in κ-type salt. The form factor $(A_\perp/\sqrt{2}A_\parallel)$ can be evaluated from hyperfine coupling tensor $\mathbf{A}$ as follows,

$$\mathbf{A} = \begin{pmatrix} a_{xx} & a_{xy} & a_{xz} \\ a_{yx} & a_{yy} & a_{yz} \\ a_{zx} & a_{zy} & a_{zz} \end{pmatrix}, \tag{7}$$

$$\left(\frac{A_\perp}{\sqrt{2}A_\parallel}\right)^2 = \frac{a_{xx}^2 + a_{yy}^2 + 2a_{xy}^2 + a_{zx}^2 + a_{zy}^2}{2a_{zz}^2}, \tag{8}$$

where the magnetic field is parallel to z-axis. We employed the mean value of the hyperfine coupling tensor of inner and outer ^{13}C cite for κ-$(ET)_2Cu(NCS)_2$ [30]. By using Eq. (6) and Eq. (8), we evaluated Korringa factor as shown in Fig. 34. Although the local spin susceptibility decreases with increasing pressure, Korringa factor increases as pressure is applied. At 3 kbar, Korringa factor shows a gradual increase. At 6 and 11 kbar, Korringa factor becomes about twice larger than that of ambient pressure, indicating the significant change of electron correlation occurs above 6 kbar.

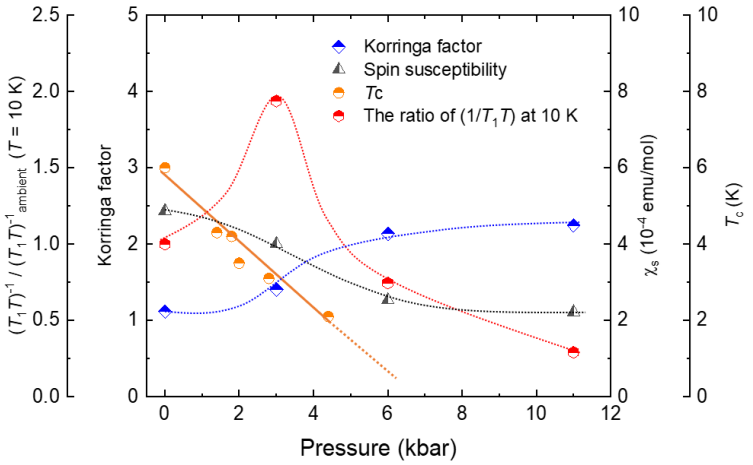

Figure 34: Temperature dependence of $1/T_1T$ at each pressures. The inset shows the result of previous study [24].

9.7 Comparison with other organic conductors

In κ-$(ET)_2Cu(NCS)_2$, Korringa factor is much greater than unity ($\mathcal{K} \approx 8$), indicating strong AF spin correlation, and decreases with increasing pressure. Moreover, Korringa factor and T_c are well correlated, implying that the AF spin correlation plays a crucial role in the emergence of superconductivity in κ-type salts [9]. In $(TMTSF)_2PF_6$, Korringa factor is almost constant even under pressures and is close to unity, indicating the weak electron correlation [26]. Instead, the strength of SDW fluctuation is well correlated to the T_c. Hence, it is likely that the SDW fluctuation is essential for the emergence of superconductivity in $(TMTSF)_2PF_6$ (Fig. 35). In λ-$(BETS)_2GaCl_4$, Korringa factor is close to unity below 3 kbar, indicating the weak electron correlation in contrast to the case of κ-$(ET)_2Cu(NCS)_2$. Remarkably, Korringa factor at 6 and 11 kbar becomes about twice larger than that of ambient pressure, indicating the significant change of electron correlation. Moreover, SC phase appears in the weak-correlated electronic state with SDW fluctuations. On the other hand, the strength of SDW fluctuation is not correlated to the T_c unlike the case in $(TMTSF)_2PF_6$. Theoretically, it has been suggested that the magnetic fluctuation can contribute to not only Cooper pair formation but also destruction [31]. Usually, T_c also depends on DOS at the Fermi energy. The DOS, which was estimated from the local spin susceptibility, is reduced about 50 % under pressure in λ-$(BETS)_2GaCl_4$. This reduction of DOS is greater than that of κ-$(ET)_2Cu(NCS)_2$ [9], suggesting the suppression of T_c under pressure in λ-$(BETS)_2GaCl_4$ is mainly governed

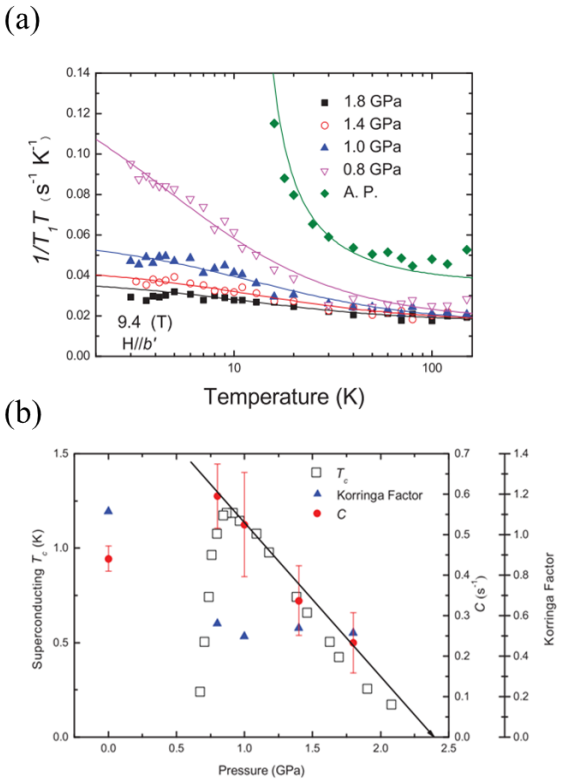

Figure 35: (a) Temperature dependence of $1/T_1T$ for $(TMTSF)_2PF_6$ measured by ^{13}C-NMR under pressure. (b) Pressure dependence of the strength of SDW fluctuation (constant C), superconducting T_c, and Korringa factor [26].

by the reduction of DOS at the Fermi energy.

These differences may originate from the difference of dimensionality and the shape of the Fermi surface. Figure 36 shows the schematic of Fermi surface for (a) $(TMTSF)_2PF_6$, (b) κ-$(ET)_2Cu(NCS)_2$, and (c) λ-$(BETS)_2GaCl_4$. $(TMTSF)_2PF_6$ and κ-$(ET)_2Cu(NCS)_2$ have simple quasi-one-dimensional (quasi-1D) and two-dimensional (2D) Fermi surface, respectively [32, 33]. On the other hand, λ-$(BETS)_2GaCl_4$ has multiple-band Fermi surfaces with quasi-1D and 2D [34, 35]. In a single-band system, the effect of pressure application is mainly widening the band width, whereas the shape of the Fermi surface can be also changed in the multiple-band system. This deformation of the Fermi surface may occur under pressure in λ-$(BETS)_2GaCl_4$, resulting in the mixing of quasi-1D and 2D Fermi surface. This can cause the significant change of the electron correlation. In this point of view, the pressure dependence of superconducting T_c seems to be related

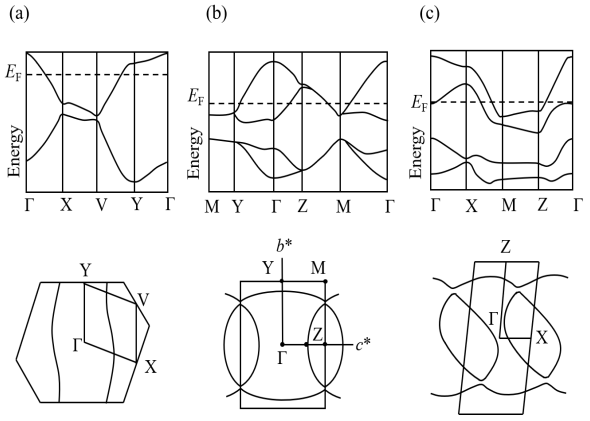

Figure 36: Schmetics of Fermi surface of (a) $(TMTSF)_2PF_6$, (b) κ-$(ET)_2Cu(NCS)_2$, and (c) λ-$(BETS)_2GaCl_4$.

to the change of electron correlation, that is, T_c is almost disappeared accompanied by the suppression of SDW fluctuations in the region where the electron correlation has changed. In addition, the development of electron correlation under pressure implies that additional AF fluctuation is appeared, which might be explained by the deformation of Fermi surface. However, our result of $1/T_1T$ did not detect such AF fluctuation; hence, it is necessary that the time scale of the additional fluctuation is much higher than the NMR frequency.

The anomalous enhancement of $1/T_1T$ under the pressure of 3 kbar can also be explained by the scenario of the deformation of Fermi surface. First, the nesting condition become suitable to SDW fluctuation under the pressure of 3 kbar. Then, the deformation of Fermi surface may disturb the nesting condition, resulting in the disappearing of SDW fluctuation under pressure. In order to investigate the change of Fermi surface under pressure, the measurement of the angular dependence of magnetoresistance oscillations is informative.

Alternative possibilities can be also considered. In $(TMTSF)_2PF_6$ and pnictide superconductor $Ba(Fe_{1-x}Co_x)_2As_2$, the temperature dependence of electric resistivity shows T-linear behavior at low temperature just above SC phase (see Fig. 38) [36]. This behavior is a typical character of non-Fermi liquid state, and theoretical studies suggest that the non-Fermi liquid state appears near a quantum critical point (QCP) [37]. This fluctuation might not be a thermal one, it might be the origin of the enhancement of $1/T_1T$ under the pressure of 3 kbar.

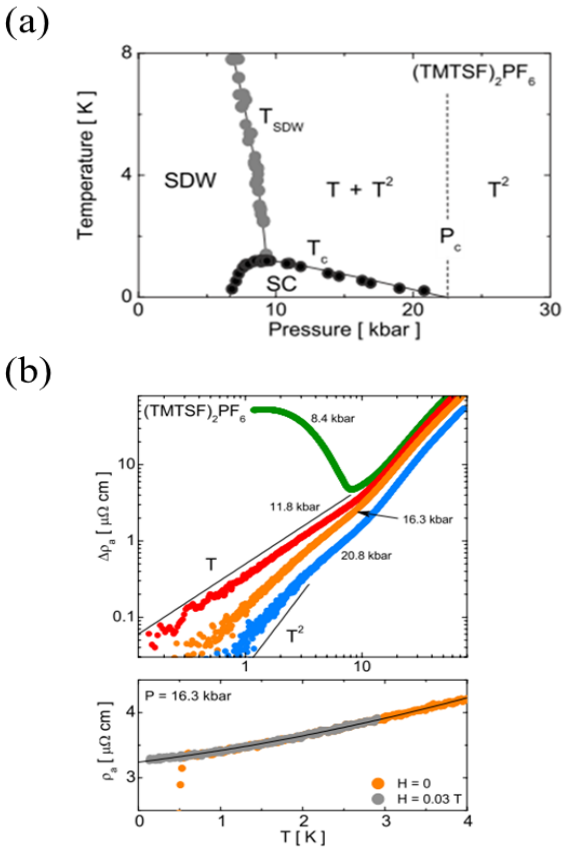

Figure 37: (a) Temperature dependence of electric resistivity for $(TMTSF)_2PF_6$. (b) Phase diagram of $(TMTSF)_2PF_6$.

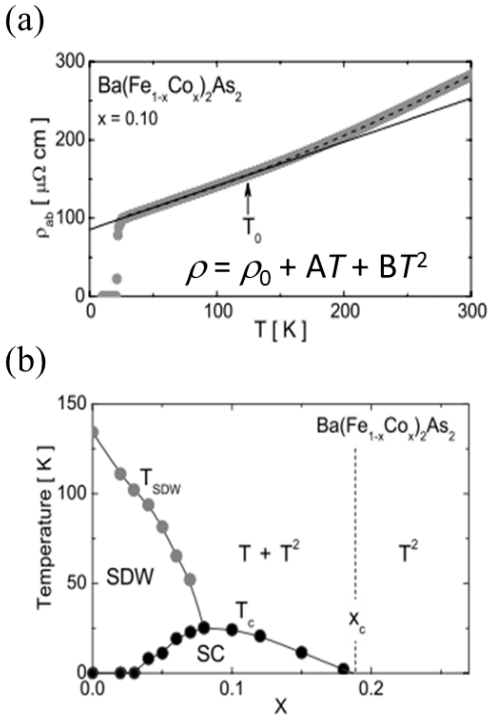

Figure 38: (a) Temperature dependence of electric resistivity for $Ba(Fe_{1-x}Co_x)_2As_2$. (b) Phase diagram of $Ba(Fe_{1-x}Co_x)_2As_2$.

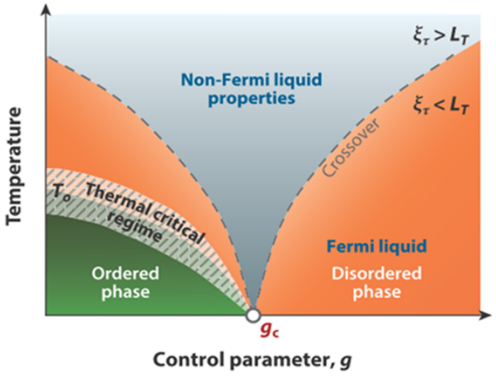

Figure 39: Schematic of typical phase diagram with quantum critical point (BCP).

10 Summary for Part. II

We have performed ^{13}C NMR measurements under pressure by using a single crystal of λ-$(BETS)_2GaCl_4$. We have found that the local spin susceptibility decreases under pressure, corresponding to the reduction of DOS at the Fermi energy. The behavior of $1/T_1T$ in the high temperature region and T^* is similar in both λ-$(BETS)_2GaCl_4$ and κ-$(ET)_2Cu(NCS)_2$, however, the strength of electron correlation is different each other. We have also confirmed that the increase of $1/T_1T$ in the low-temperature region which can be attributed to the SDW fluctuation. Unlike the case in $(TMTSF)_2PF_6$, the increase of $1/T_1T$ is significantly enhanced under the pressure of 3 kbar, implying the enhancement of SDW fluctuation. Whereas, the increase of $1/T_1T$ at low temperature is reduced at 6 kbar and is completely suppressed at 11 kbar. Moreover, Korringa factor is increased above 6 kbar, indicating the significant change of the electron correlation. This behavior differs from that for κ-$(ET)_2Cu(NCS)_2$ and $(TMTSF)_2PF_6$, and this can be attributed to the multi-band system of Fermi surface. The suppression of SDW fluctuation is likely related to the change of electron correlation under pressure. We revealed that the superconductivity appears in the weak-correlated electronic state with SDW fluctuations. The contribution of SDW fluctuation to SC is still controversial, so that further experimental and theoretical research is required.

Part III

Coupling of molecular motion and electronic state of organic molecular dimer Mott insulator β'-$(ET)_2ICl_2$ proved by ^{1}H- and ^{13}C-NMR

11 Introduction

Recently, the dielectric property of organic molecular crystals is attracting considerable interest since they show novel ferroelectric properties owing to charge displacements that are driven by various phase transitions [38,39]. The large ferroelectric polarization in TTF-CA [TTF = tetrathiafulvalene and CA = *p*-chloranil] is induced by a neutral-to-ionic transition [40,41]. Moreover, the ferroelectricity observed in $(TMTTF)_2X$ is caused by charge ordering [42,43]. Interestingly, the ferroelectric nature of dimer Mott insulators consisting of ET has also been demonstrated [44–47]. For example, both the quasi-two-

dimensional organic molecular crystals κ-$(ET)_2Cu_2(CN)_3$ and β'-$(ET)_2ICl_2$ show large anomalies in the temperature dependence of the dielectric constant as well as ferroelectric relaxor-like behaviors. These imply the interacting electric dipole in a dimer and the origin of the charge degrees freedom is one of the interesting problem. In κ-$(ET)_2Cu_2(CN)_3$ salts, it has been suggested that the origin of the dielectric anomaly is attributed to the disorder of anion layer. The disorder in anion layers induce a random potential on ET layers, and produce a large-scale charge inhomogeneity and domain walls [48]. In contrast, β'-$(ET)_2ICl_2$ does not have a disorder in anion layer. Moreover, the temperature regions that the dielectric anomaly is observed are different between κ-$(ET)_2Cu_2(CN)_3$ and β'-$(ET)_2ICl_2$. These indicate that the origin of the dielectric anomaly is different for both materials although the behavior of the dielectric constant is similar. Some possibele scenario has been suggested for the dielectric anomaly of β'-$(ET)_2ICl_2$, however, the origin is still under discussion. In this study, we have investigated the origin of the dielectric anomaly in β'-$(ET)_2ICl_2$.

11.1 Crystal structure and P-T phase diagram of β'-$(ET)_2ICl_2$

Figure 40 shows the crystal structure of β'-$(ET)_2ICl_2$. Lattice parameters and space group are summarized in Table 1.1 [49]. This salt consists of two kinds of layer, one is conduction layer of ET molecules, the other is insulating layer of ICl_2 anions. These layers are stacked alternately parallel to the a^* axis (perpendicular to bc plane). Due to the β'-type donor arrangement, two ET molecules form a dimer in a crystal as shown in Fig. 41. Figure 42 shows the pressure-temperature phase diagram of β'-$(ET)_2ICl_2$. This material has an antiferromagnetic transition at $T_N = 22$ K under ambient pressure [3]. The ground state of this material is a dimer Mott insulationg phase with antiferromagnetic ordering. Also, this salt shows a superconducting transition at $T_C = 14.2$ K under pressure 8.2 GPa [50]. This is known as the highest T_C among the ET based organic superconductors.

11.2 Dimer Mott insulator

In κ- and β'-type salts, two ET molecules form a dimer in the crystal. Since the formal valence of ET is +0.5, each dimer has one hole carrier on average. If we employ the dimer picture, the electronic state is considered to possess an effective half-filled system. When the dimerization occurs, the molecular orbitals split into the bonding and the anti-bonding orbitals as shown in Fig. 43. The characteristics of a dimerized half-filled system can be explained by the Hubbard model. In the simplest case, we can consider

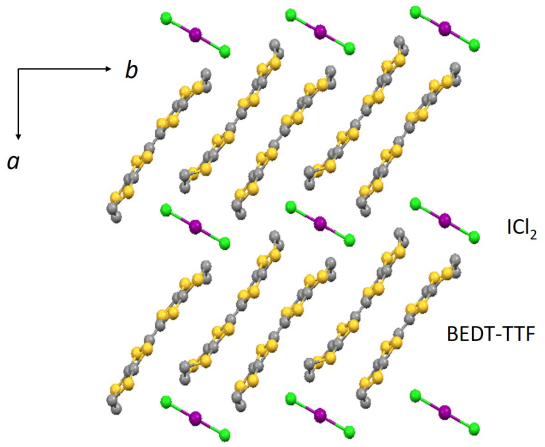

Figure 40: Crystal structure of β'-$(ET)_2ICl_2$.

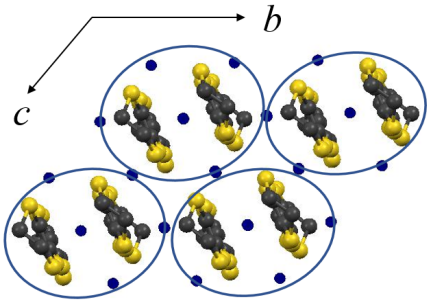

Figure 41: Dimerization of ET molecules viewed along the long axis of the ET molecule. The crosed circles represent the inversion centers.

Table 1: The space group and the lattice parameters of β'-$(ET)_2ICl_2$.

Lattice	Triclinic
Space group	$P\bar{1}$
a [Å]	12.937(3)
b [Å]	9.778(2)
c [Å]	6.636(1)
α [°]	98.59(2)
β [°]	100.9882)
γ [°]	87.19(2)
V [Å^3]	814.6(3)

the eletronic system with only two parameters. One is on-site Coulomb repulsion (U) and the other is interdimer transfer integral (t) which is proportional to the bandwidth (W), where W represents the mobility of a carrier between dimers. The on-site Coulomb repulsion can be calculated by following equation [51];

$$U = \frac{U_{\mathrm{ET}}}{2}\left(1 - \sqrt{1 + \frac{4t_d}{(U_{\mathrm{ET}})^2}}\right) \sim 2t_d - \frac{4t_d^2}{U_{\mathrm{ET}}}, \tag{9}$$

where U_{ET} represents the on-site Coulomb repulsion on a ET molecule. When we use an approximation $U_{\mathrm{ET}} >> t_d$, where t_d is intradimer transfer integral, we can obtain the relation $U \sim 2t_d$. Hence, the electronic state of a dimeric conductors can be predicted by the competition of U and t. When $U >> t$, the carrier is localized on the dimer and the material becomes an insulator (Mott transition), which is called a dimer Mott insulator.

11.3 Dimer Mott insulating phase of β'-$(ET)_2ICl_2$

β'-$(ET)_2ICl_2$ is a well-established dimer Mott insulator at ambient pressure. Due to the β'-type donor arrangement, strong dimerization is realized in β'-$(ET)_2ICl_2$ at ambient pressure, which is supported by the calculations of the intermolecular transfer integral [49]. When a dimerization is strong, that is, the intradimer transfer integral (t_d) is larger than interdimer transfer integrals (t), the on-site Coulomb repulsion (U) becomes larger than the interdimer transfer integrals (t) because U is approximately proportional to the intradimer transfer integral (t_d). Thus, the charge is strongly con-

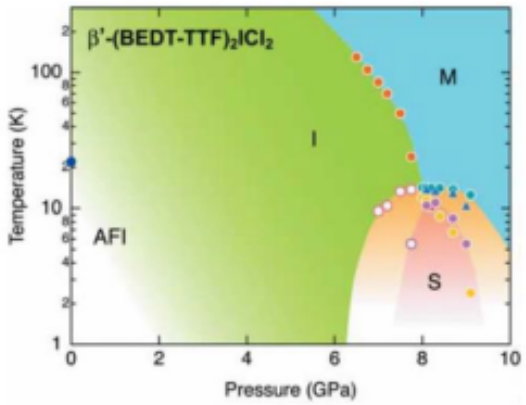

Figure 42: P–T phase diagram of β'-$(\mathrm{ET})_2\mathrm{ICl}_2$.

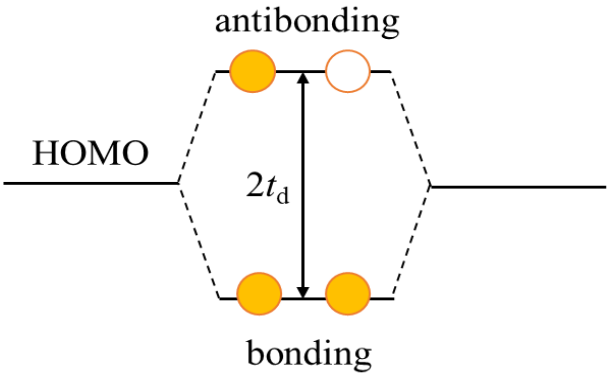

Figure 43: Schematics of the electronic state of a dimer.

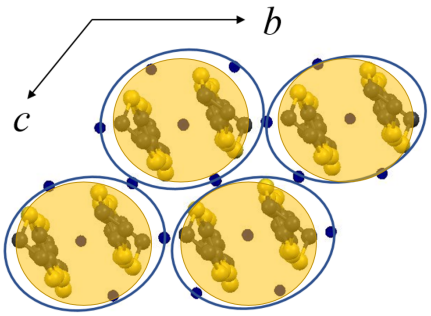

Figure 44: Schematic of the homogeneous charge distribution in a dimer.

fined on a dimer, resulting in the insulating phase of β'-$(ET)_2ICl_2$. Moreover, ^{13}C-NMR measurement and the Curie constant of the paramagnetic phase at high temperature show that spin per dimer is $S = 1/2$ [52]. This supports that this salt has a localized spin system. Indeed, the antiferromagnetic transition occurs at $T_N = 22$ K since there are antiferromagnetic exchange interaction (J_{AF}) among the localized spins [3]. These magnetic properties also embody that β'-$(ET)_2ICl_2$ is a typical dimer Mott insulator that has large U/t value.

11.4 Charge degrees of freedom in a dimer Mott insulating phase

From its crystallographic symmetry, β'-$(ET)_2ICl_2$ belongs to the space group $P\bar{1}$ [49]. There is an inversion symmetry at the center of the dimer, which is represented by the closed circles in Fig. 41. Due to this inversion symmetry, two ET molecules in a dimer are crystallographically equivalent. Therefore, the charge in the dimer should be equally distributed between the two ET molecules as shown in Fig. 44. Hence, the possibility of static charge degrees of freedom in the dimer Mott insulating phase has not been discussed. However, it has been reported that β'-$(ET)_2ICl_2$ shows a relaxor-like ferroelectric behavior in the dielectric constant around 100 K. Moreover, the field-induced charge disproportionation (CD) has been demonstrated by Raman scattering measurement under electric fields. These experiments indicate that the charge degrees of freedom appear even in the dimer Mott insulating phase and the inversion symmetry in the dimer is broken.

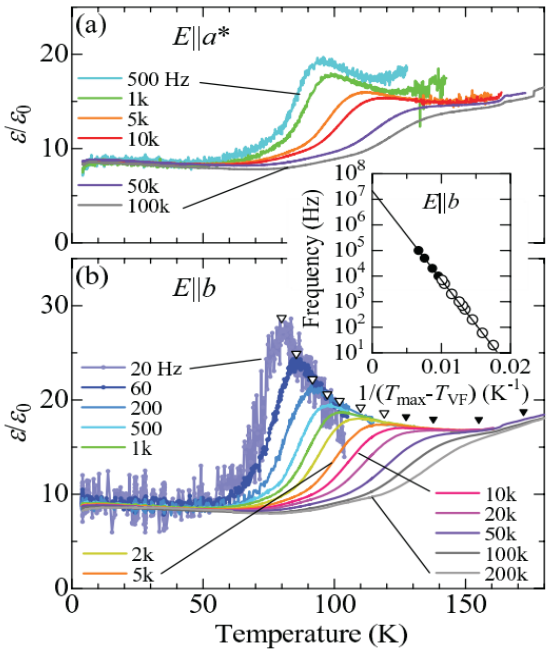

Figure 45: Temperature dependence of the dielectric constant of β'-$(ET)_2ICl_2$ [44].

11.5 Dielectric Properties of β'-$(ET)_2ICl_2$

Figure 45 shows the temperature dependence of the dielectric constant of β'-$(ET)_2ICl_2$ [44]. The temperature dependence of the dielectric constant has significant frequency dependence and shows a relaxor-like ferroelectric behavior. When electric fields were applied parallel to the b axis (the stacking direction of the dimers), larger peaks were observed in the dielectric constant. This implies that charge disproportionation (CD) occurs in the dimer as shown in Fig. 46. Iguchi *et al.* suggest that the antiferromagnetic interaction among the spins may play a crucial role for the appearance of the charge degrees of freedom in the dimer. However, the origin of the dielectric anomaly is still under discussion.

11.6 Field-induced CD state of β'-$(ET)_2ICl_2$

In addition to the anomalies in the dielectric constant, the field-induced CD state has also reported by Hattori *et al.* [45]. They performed Raman scattering measurement under electric fields. Figure 47(a) shows the temperature dependence of the Raman spectra in (cc) polarization under zero electric field. Here, (cc) denotes that the polar-

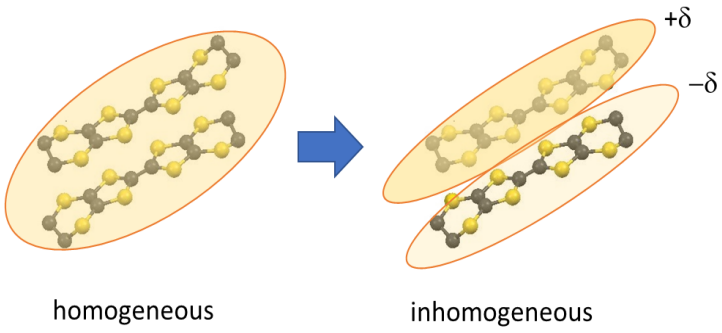

Figure 46: Schematics of the charge degrees of freedom in a dimer.

izations of the incident light and the detected light were both set parallel to the c axis. Below 200 K, three peaks were observed which can be assigned to the charge-sensitive vibrational ν_2, ν_3, and ν_{27} mode (see Fig. 48) [53]. Raman shift of ν_2 mode is simply related to the valence of ET molecule (ρ) and obeys following relation;

$$\nu_2(\rho) = 1447 + 120(1 - \rho)\ \mathrm{cm}^{-1}. \tag{10}$$

Using this relation, the valence of ET molecule was calculated as $\rho = +0.56$. This is reasonable value because the formal valence of the ET dimer is +1. Figure 47(c) shows the Raman spectra under several electric fields. When the electric field of 5 kV/cm is applied, two additional peaks were observed at both sides of ν_2 mode. From the peak position of additional peaks, 1492 and 1510 cm^{-1}, the valences of the ET molecules were calculated as $\rho = +0.625$ and $+0.475$, respectively. This indicates that a +0.075 charge is transferred from one ET to another within a dimer. This valence change suggests that charge imbalance in the distribution of electric charge in a dimer, namely, intradimer CD, occurs. The authors applied high electric field of 10 kV/cm to another sample, the obtained spectra are shown in Fig. 47(d). The magnitude of the additional peaks were increased and that of central peak was suppressed, but their peak positions have not been changed. This indicates that the extent of the charge transfer is independent of the applied electric field.

Hattori *et al.* have also found that the CD state was maintained after they removed the electric field, indicating that the CD state is stable. Moreover, their further experiments indicate that there is a barrier between non-CD and CD states as shown in Fig. 49. Center valley represents the Mott insulating state, in which the charge is equally distributed to the two ET molecules. The left and right valleys correspond to the CD

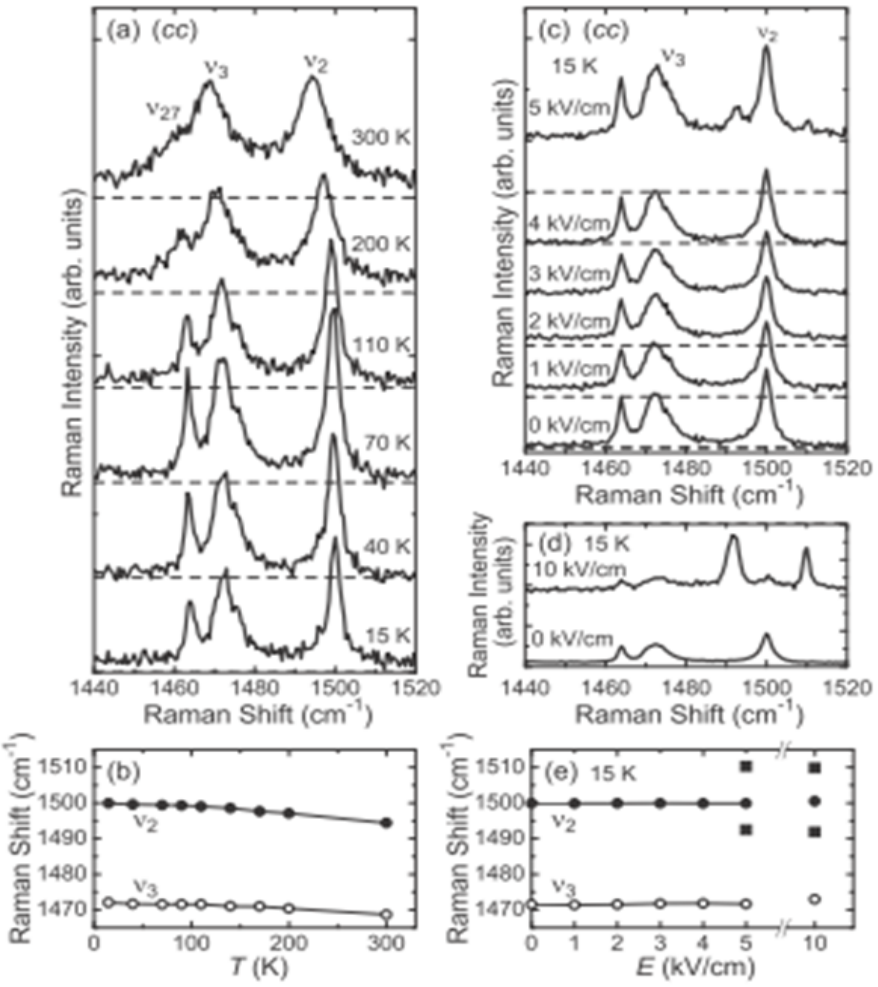

Figure 47: (a) Temperature dependence of the Raman spectra under zero field [45]. (b) The Raman shift of ν_2 and ν_3 modes under zero field. (c) Raman spectra under several electric fields at 15 K. (d) The Raman spectra under high electric field at 15 K. (e) Raman shift ν_2 and ν_3 modes under several electric fields.

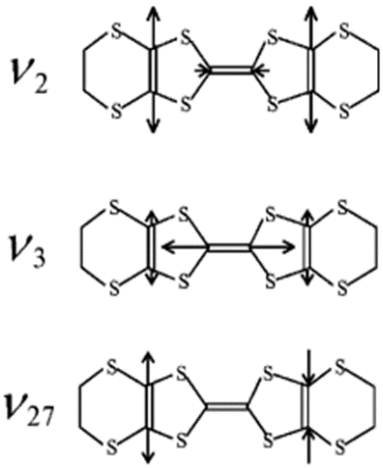

Figure 48: Schematics of the Raman active vinrational modes ν_2 and ν_3 and the Raman inactive vibrational mode ν_{27}.

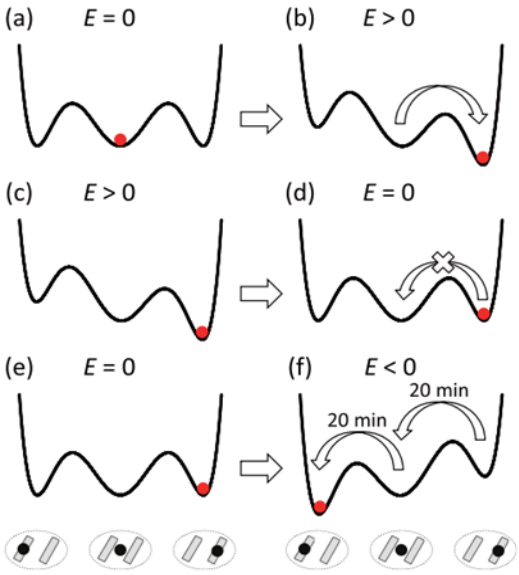

Figure 49: Schematics of the three valley model.

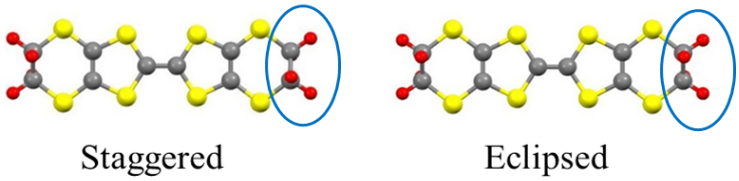

Figure 50: Two stable conformations of the ethylene group of ET molecule.

state in which the charge is distributed disproportionally.

12 Motivation

12.1 Background

As we have seen so far, the novel dielectric properties have been demonstrated in a dimer Mott insulator β'-$(ET)_2ICl_2$. In this salt, the charge degrees of freedom are not expected to be appear in a dimer Mott insulating phase because the charge should be equally distributed to two ET molecules in a dimer due to the inversion symmetry. However, it has not been unraveled the mechanism of the appearance of the charge degrees of freedom in a dimer.

12.2 Ethylene motion

One possibility that can produce the charge degrees of freedom in the Mott insulating phase is "ethylene motion". The terminal ethylene group of ET molecule has two stable conformations, namely, eclipsed and staggered, as shown in Fig. 50 [54–57]. At high temperatures, the ethylene groups are fluctuated between these two conformations. This thermal molecular motion is known as the ethylene motion. In several ET salts, it has been confirmed that the slowing down of the ethylene motion occurs and affect their physical properties.

12.3 Ethylene motion in κ-type salts

Figure 51 shows the temperature dependence of the resistivity of κ-$(ET)_2Cu(NCS)_2$ [58]. At ambient pressure, a semi-conductor-like behavior is observed above 100 K, and a metal-insulator (M-I) transition occurs at around 100 K. In addition, the M-I transition disappears by applying pressure. In κ-type ET salts such as κ-$(ET)_2Cu(NCS)_2$ and

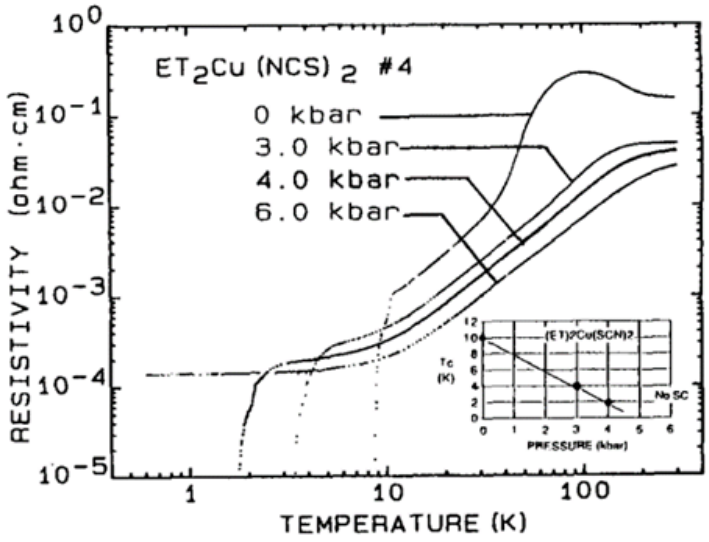

Figure 51: The temperature dependence of the resistivity of κ-$(ET)_2Cu(NCS)_2$ sallt under several pressure.

κ-$(ET)_2Cu[N(CN)_2]Cl$, the slowing down of the ethylene motion has been confirmed at around 100 K from ^1H NMR measurement [59, 60]. Moreover, Matsumoto and Kuwata *et al*. revealed that the ehtylene motion scatters conducting electrons above 100 K, resulting in the semi-conducting behavior in those salts [54, 55]. Also, the slowing down of the ethylene motion occurs at around 100 K, which reduces the scattering of conducting electrons. As aresult, the M-I transition occurs at around 100 K. They have also confirmed that the ethylene motion disappears when they applied pressure. This is consistent with the disappearing of the M-I transition under pressure. These experiments indicate that the ethylene motion is coupled to the electronic system and affects the physical property. The ground state of κ-type salts are metallic, hence, the ethylene motion affects the conductivity. In contrast, β'-$(ET)_2ICl_2$ is a well-established dimer Mott insulator. Therefore, the ethylene motion can affect its dielectric property.

12.4 The possible scenario of the charge degrees of freedom due to the ethylene motion

As mentioned above, the charge is strongly confined on a dimer in the dimer Mott insulating phase and is equally distributed to each molecule due to the inversion symme-

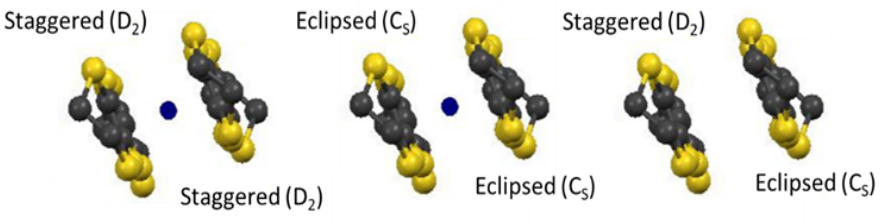

Figure 52: The schematics of the possible origin of the charge degrees of freedom in a dimer.

try. For realization of the charge degrees of freedom, the symmetry breaking is required. The two kinds of conformations of the ethylene group "staggered" and "eclipsed" have different symmetry (D_2) and (C_S), respectively. Therefore, if one ET is staggered and the other one is eclipsed in the dimer, the inversion symmetry at the center of the dimer should be broken as shown in Fig. 52. In this case, the charge in the dimer should be no longer equally distributed to the ETs, rather, the inhomogeneous charge distribution can be realized. Therefore, we focused on the ethylene motion as a possible origin of the dielectric anomaly.

12.5 Purpose of our study

In this study, we have performed ^{1}H-NMR measurement which is sensitive to the proton dynamics to investigate the slowing down of the ethylene motion in β'-$(ET)_2ICl_2$. Moreover, we have performed ^{13}C-NMR measurement to unravel the relationship between the ethylene motion and the electronic state.

13 Experiments

13.1 Ethylene motion and ^{1}H-NMR study

13.1.1 Anomaly in the spin-lattice relaxation time

The slowing down of the ethylene motion has been observed in several ET salts such as κ-$(ET)_2Cu(NCS)_2$, κ-$(ET)_2Cu[N(CN)_2]Cl$, and β-$(ET)_2I_3$ [59–61]. In these salts, an anomaly in the spin-lattice relaxation time T_1 in ^{1}H-NMR measurement has been observed as shown in Fig. 53. From 10 to 100 K, T_1 obeys the Korringa law, which correspond to the metallic behavior of κ-$(ET)_2Cu(NCS)_2$. Below 10 K and above 100 K,

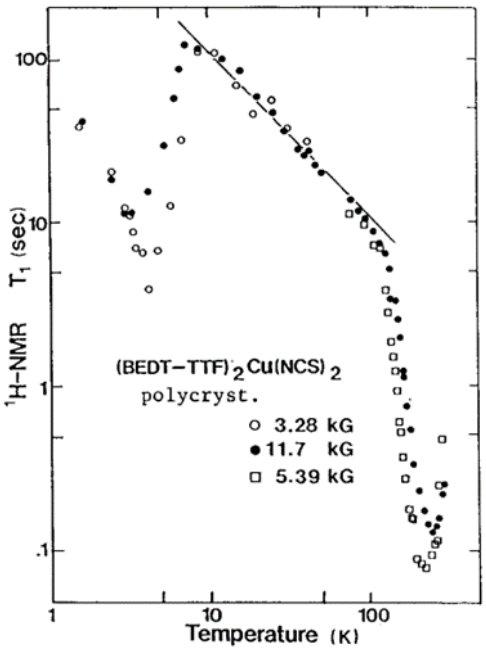

Figure 53: The temperature dependence of the spin-lattice relaxation time T_1 for κ-$(ET)_2Cu(NCS)_2$ measured by ^{1}H-NMR.

anomalous peaks were observed. Note that the anomaly below 10 K is ascribed to the antiferromagnetic fluctuation. On the other hand, the behavior of T_1 above 100 K can be explained by the Bloembergen-Pound-Purcell model [62].

13.1.2 Bloembergen-Purcell-Pound (BPP) theory

In 1948, Bloembergen *et al.* published the paper on a magnetic relaxation which originates from the magnetic fluctuation dirived by molecular motion. If we consider the molecular motion of a H_2O molecule, not only the magnetic fluctuation on a proton nuclei but the dipole-dipole coupling affects the magnetic relaxation. According to the BPP theory, spin-lattice relaxation time T_1 due to molecular motion can be described as the following equation;

$$\frac{1}{T_1} = C\left(\frac{\tau_c}{1+\tau_c^2\omega^2} + \frac{4\tau_c}{1+4\tau_c^2\omega^2}\right), \tag{11}$$

where τ_c is the correlation time of the molecular motion and C is a constant. The second term represent the effect of the magnetic relaxation due to nuclear dipole-dipole inter-

action. The BPP formula has a maximum when $\omega\tau_c = 0.616$. This makes a significant dependence in a magnitude of a peak of BPP curve. In other words, a relaxation time T_1 should have a magnetic field dependence if there is a molecular motion.

13.1.3 Ethylene motion and the BPP model

We can apply the BPP model to the case of ethylene motion. Proton nuclei in the ethylene groups are fluctuated depending on the temperature, and can trigger the magnetic relaxation. As shown in Fig. 53, the magnitude of peaks in T_1 above 100 K decreases with increasing the magnetic field. This is the feature of the BPP model, which indicates the existence of the slowing dynamics of the ethylene motion. Kuwata *et al.* assumed that the correlation time obeys the Arrhenius function [54];

$$\tau_c = \tau_0 \exp(\Delta E/k_B T), \tag{12}$$

where ΔE is an activation energy between the eclipsed and the staggered conformation, τ_0 is the high temperature limit of the correlation time, and k_B is the Boltzmann constant. Kuwata *et al.* conducted the fitting by using eqs. (1.6) and (1.7). According to their fitting, the fitting parameters are estimated as $\Delta E \sim 1500$ K, $\tau_0 \sim 10^{-11}$ s.

13.2 Sample preparation and experimental condition

13.2.1 Sample preparation

β'-$(ET)_2ICl_2$ was synthesized by using an electrochemical method [63]. ET and TBA-ICl_2 was dissolved in THF. The solution was sealed into a cell with argon gas, and a weak current of the order of 1 μA was flowed to the solution during a few weeks. Plate-like samples were obtained after the oxidization.

13.2.2 Conditions for ^{1}H-NMR

Polycrystalline samples were used for ^{1}H-NMR, which is stuffed into a glass tube. The edges of the glass tube are sealed with a proton free grease. We performed ^{1}H-NMR measurement under magnetic fields of 0.55, 1.14, and 2.00 T. NMR spectra were obtained by fast Fourier transformations (FFTs) of the echo signal. We determined the spin-lattice relaxation time T_1 using the saturation-recovery method.

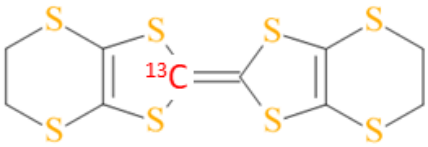

Figure 54: BEDT-TTF molecule in which the one side of C=C bond was enriched with ^{13}C nuclei.

13.2.3 Conditions for ^{13}C-NMR

For ^{13}C NMR, a plate-like single crystal was used. To prevent the Pake-doublet problem, we enriched the one side of C=C bond with ^{13}C nuclei by using the cross-coupling method [64, 65] as shown in Fig. 54. The magnetic field of 9.4 T was applied parallel to the a axis. We defined the spin-spin relaxation time T_2 as the rate corresponding to Lorentz decay.

14 Results and Discussion

14.1 ^{1}H NMR measurement

Figure 55 shows the temperature dependence of the ^{1}H-NMR spectra under magnetic field of 0.55 T. The horizontal axis represents the shift from the central frequency $f =$ 23.46 MHz. One peak is observed at each temperature and there is no significant change in the spectra.

Figure 56 shows the temperature dependence of the T_1^{-1} in ^{1}H-NMR at several magnetic fields. Peaks were observed at 273, 287, and 300 K in magnetic fields of 0.55, 1.14, and 2.00 T, respectively. The peaks shift to high temperatures and decrease in magnitude with an increase in magnetic field. Below 200 K the T_1^{-1} converges to a same value, regardless of the applied magnetic field. Similar field-dependent behavior of the peak structure in T_1^{-1} has been observed in other ET salts, such as β-$(ET)_2I_3$, κ-$(ET)_2Cu[N(CN)_2]Cl$, and κ-$(ET)_2Cu(NCS)_2$. In these salts, it is well established that the field-dependent behavior can be explained by the Bloembergen-Purcell-Pound (BPP) model [62] and is attributed to the slowing down of the ethylene motion. The BPP model treats the magnetic fluctuations induced by molecular motions via a dipole-dipole interaction. Since the terminal ethylene groups are thermally fluctuated, the local fields at proton sites in those groups fluctuate, which can affect the magnetic relaxation of the protons. With a decrease in temperature, the correlation time of the ethylene motion

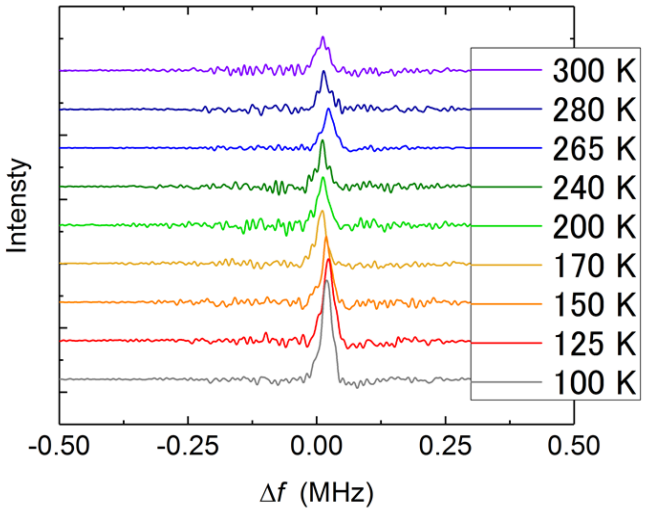

Figure 55: ^{1}H-NMR spectrum under several magnetic fields.

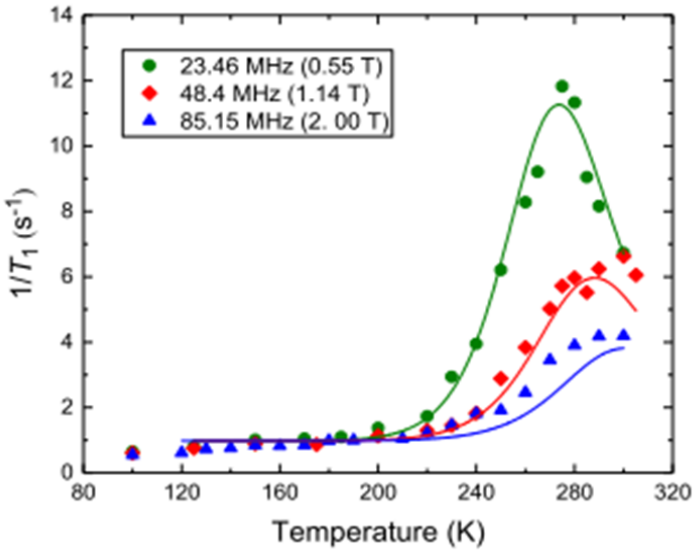

Figure 56: The temperature dependence of the spin-lattice relaxation rate $^1T_1^{-1}$

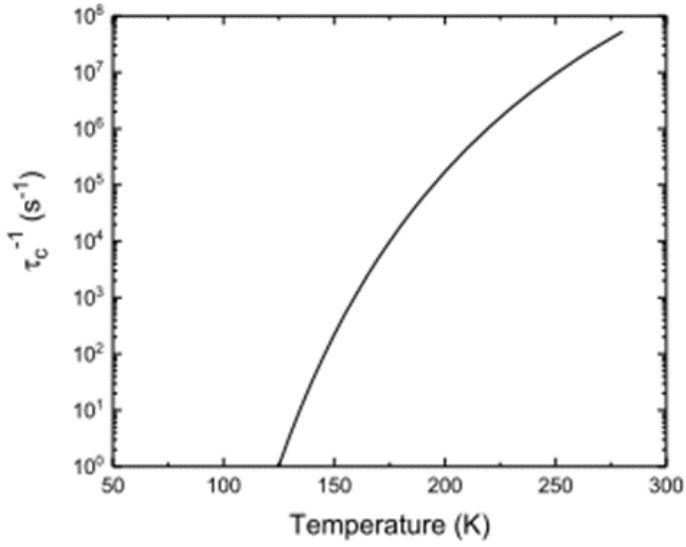

Figure 57: The temperature dependence of the inverse correlation time τ_c^{-1} (the time scale of the ethylene motion).

increases. Roughly, a peak is observed in the T_1^{-1} when the timescale of the ethylene motion becomes the same as the order of the NMR resonance frequency . These behaviors can be explained well by the BPP model. Note that not only does the molecular motion contribute to the magnetic relaxation but it also does the antiferromagnetic fluctuation of the localized electrons. However, the contribution of the antiferromagnetic fluctuation to the T_1^{-1} is very small and is almost constant at high temperatures. Therefore, we add a constant term a to Eq. (11), thus obtaining the following equation:

$$\frac{1}{T_1} = C\left(\frac{\tau_c}{1+\tau_c^2\omega^2} + \frac{4\tau_c}{1+4\tau_c^2\omega^2}\right) + a. \tag{13}$$

We obtained the solid lines in Fig. 56 by fitting the BPP model to the data using Eqs. (12) and (13). The temperature dependence of T_1^{-1} can be explained by the BPP model using the fitting parameters $\Delta E \sim 4000$ K, $\tau_0 \sim 10^{-14}$ s, $C \sim 10^8$ s^{-2}, and $a \sim 0.98$ s^{-1}. Using these parameters and Eq. (12), we can calculate the temperature dependence of τ_c, as shown in Fig. 57.

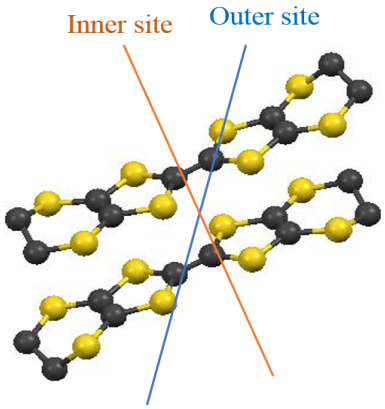

Figure 58: The definition of the crystallographycally nonequivalent inner and outer ^{13}Csites.

14.2 ^{13}C-NMR measurement

We confirmed the existence of the slowing down of the ethylene motion in β'-$(ET)_2ICl_2$ from ^{1}H-NMR measurement. The next interest is whether the ethylene motion is coupled to the electronic system in this salt. In order to unravel the relationship between the ethylene motion and the electronic system, we have performed ^{13}C-NMR, where ^{13}C is strongly coupled to the π electron of ET that can affect the physical property. As shown in Fig. 58, there are two crystallographically nonequivalent inner and outer ^{13}C sites in a BEDT-TTF dimer. Therefore, two peaks are expected to be observed in a ^{13}C-NMR. As shown in the inset of Fig. 59, two distinct peaks were observed in ^{13}C-NMR spectra, which corresponds to the inner and outer ^{13}C sites. Figure 59 shows the temperature dependence of the linewidth of both inner and outer site. Anomalous developments in linewidth were observed at around 150 K for both sites. Note that the large increase below 50 K is ascribed to the antiferromagnetic fluctuation. The anomalous increments around 150 K for the outer site is 2.7 times larger than that of the inner site, indicating a significant site dependence. In order to unravel which part is dominant, we have measured the temperature dependence of spin-spin relaxation time T_2.

Figure 60 shows the temperature dependence of the spin-spin relaxation rate T_2^{-1}. The distinct anomaly was observed at around 150 K for both the inner and the outer sites. The anomalous increments for the inner and outer site are comparable to that of the linewidth. This indicates that the anomaly in the linewidth is attributed to

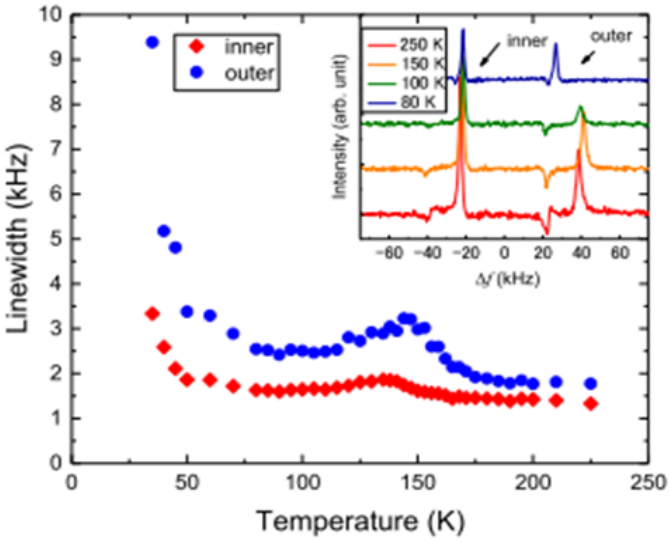

Figure 59: The temperature dependence of the linewidths of ^{13}CNMR spectra. The inset shows the ^{13}C-NMR spectra at several temperatures.

the T_2 anomaly, i.e., slow magnetic fluctuation at the ^{13}C nuclei. Contribution to T_2^{-1} come from magnetic fluctuations parallel to the external field with slow frequencies. One of them is due to the spin-spin coupling between ^{13}C nuclei which does not show significant temperature dependence. The other one is due to the ethylene motion with the correlation time τ_c. As shown in Fig. 57, time scale of the ethylene motion at around 150 K is the order of 1 kHz. This is consistent with the time scale of T_2^{-1}. Therefore, the anomaly in T_2^{-1} can be attributed to the ethylene motion.

14.3 Coupling mechanism between the ethylene motion and ^{13}C nuclei

We have confirmed the anomalies in the linewidth of NMR spectra and T_2^{-1} are attributed to the slow dynamics of the ethylene motion. In this section, we consider the coupling mechanism between the ethylene motion and ^{13}Cnuclei. From the spectral density function of ethylene motion $J(\omega)$, the T_2^{-1} on α site can be described as following function;

$$\left(\frac{1}{T_2}\right)_\alpha = \int_0^\Delta \{D_\alpha^2 J(\omega) + A_\alpha^2 J(\omega)\} d\omega. \tag{14}$$

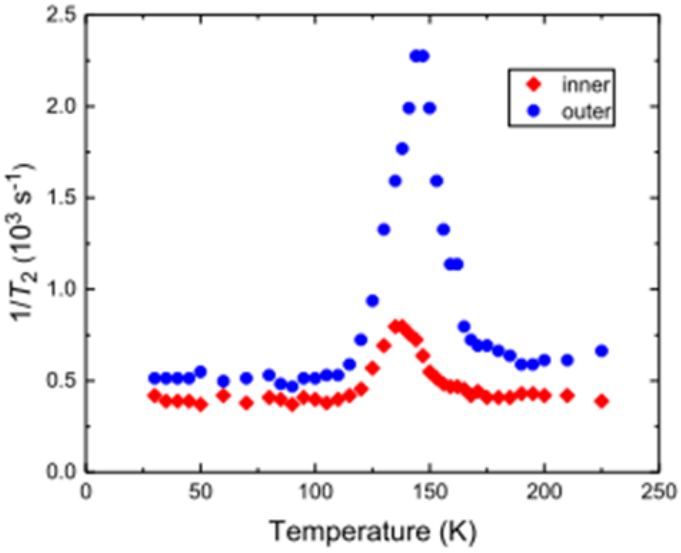

Figure 60: The temperature dependence of the spin-spin relaxation rate $^{13}T_2^{-1}$.

The first term in the integral represents the direct coupling effect which originates from the dipole-dipole interaction between ^{1}H and ^{13}Cas shown in Fig. 61. D_α is the coupling constant between ^{1}H and ^{13}C nucleus. The second term corresponds to the indirect coupling effect which originates from the modulation of molecular orbital due to the ethylene motion as shown in Fig. 62. In the direct coupling, the energy of dipole-dipole interaction is proportional to r^{-3}, where r is the distance between ^{1}H and ^{13}C nucleus. In ET molecule, r is relatively large, therefore, the effect of dipole-dipole interaction should be small. Moreover, the distances between ^{1}H nucleus and ^{13}C nuclei of inner and outer site are not so different. Hence, the site dependence of the anomalies in the linewidth and T_2 cannot be explained by the direct coupling effect. On the other hand, the indirect coupling is come from the interactions between charge on molecule and ^{13}C nuclei. In this case, T_2^{-1} should be proportional to the square of hyperfine coupling constant A_α of each inner and outer site [55, 66].

Eto *et al.* previously determined the hyperfine coupling constant of both the inner and outer site [52]. According to them, the ratio of the hyperfine coupling constant of the outer site to the inner site is evaluated as ~ 3. We estimated the ratio of the anomalous increments for the outer site to the inner site as 2.7 and 4.3 for the linewidth and T_2^{-1}, respectively. Therefore, the anomalies in the linewidth and the T_2^{-1} is clearly related to the hyperfine coupling constant. This indicates that the ethylene motion modulates the

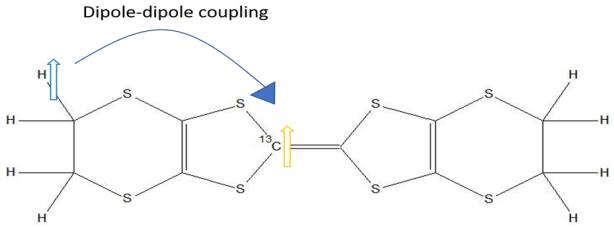

Figure 61: The schematic of the direct coupling mechanism.

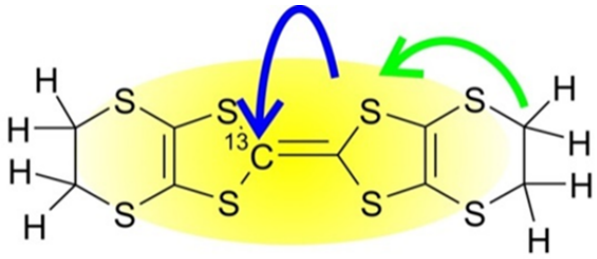

Figure 62: The schematic of the indirect coupling mechanism.

molecular orbital of BEDT-TTF molecule, and generate the slow magnetic fluctuation at the ^{13}C nuclei. Hereby we confirmed the significant coupling between the ethylene motion and the electronic system in β'-$(ET)_2ICl_2$.

14.4 The possible origin of the electric dipole in a dimer

As discussed above, the ethylene groups can possess either a staggered or an eclipsed conformation and the ethylene motion modulates the electronic state. Depending on the conformation, the molecular orbital of the BEDT-TTF molecule can be modulated, thus producing a significant energy gap $\Delta\epsilon$ in the highest occupied molecular orbital (HOMO). From theoretical calculations, $\Delta\epsilon$ is estimated to be of the order of 10 meV [54, 57, 67]. The modulation of $\Delta\epsilon$ triggers the indirect coupling between the ethylene motion and the local field. In addition, from band-structure calculations and infrared (IR) absorption measurements, the intradimer transfer integral (t_d) is estimated to be 250 meV [68, 69]. Thus, $\Delta\epsilon$ is large enough to affect the electronic state in a dimer. Therefore, we consider the possible emergence of charge degrees of freedom due to the ethylene motion. The electronic state in a dimer (Ψ_{dimer}) can be described as a linear combination of the wave functions of the two BEDT-TTF molecules in the dimer, ψ_1 and ψ_2. It can be represented by the following equation:

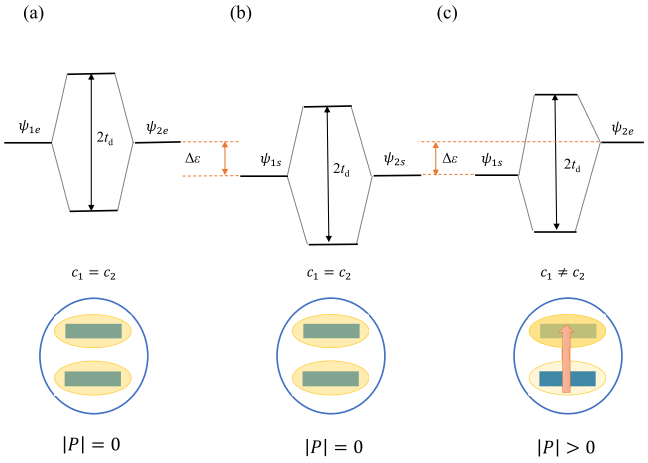

Figure 63: The schematic diagram of the electronic state of a dimer.

$$\Psi_{\text{dimer}} = c_1\psi_1 + c_2\psi_2 \tag{15}$$

As shown in Figs. 63(a) and 63(b), if the ethylene group of both ET molecules in the dimer possesses the same conformation either staggered or eclipsed, the coefficients c_1 and c_2 are equal owing to inversion symmetry at the center of the dimer. In this case, a CD state does not occur. However, if one ET molecule is in a staggered conformation, while the other is in an eclipsed conformation, then c_1 and c_2 are no longer equal, and a CD state can develop in the dimer, as shown in Fig. 63(c). Let us define the wave function of a molecular orbital of ET in a staggered or an eclipsed conformation as ψ_{is} or ψ_{ie} $(i = 1, 2)$, respectively. The extent of charge transfer in the dimer can be determined by using the parameters $\Delta\epsilon$ and t_{d}. If the Hamiltonian $(\mathcal{H})$ includes the intradimer interaction, we obtain the following secular equation:

$$\begin{bmatrix} \langle\psi_{1e}|\,\mathcal{H}\,|\psi_{2e}\rangle & \langle\psi_{1e}|\,\mathcal{H}\,|\psi_{2s}\rangle \\ \langle\psi_{1s}|\,\mathcal{H}\,|\psi_{2e}\rangle & \langle\psi_{1s}|\,\mathcal{H}\,|\psi_{2s}\rangle \end{bmatrix} \Psi_{\text{dimer}} = E\Psi_{\text{dimer}}, \tag{16}$$

where $\Psi_{\text{dimer}} = c_1\psi_{1\alpha} + c_2\psi_{2\beta}$ $(\alpha, \beta = e \text{ or } s)$. The off-diagonal elements $\langle\psi_{1e}|\,\mathcal{H}\,|\psi_{2s}\rangle$ and $\langle\psi_{1s}|\,\mathcal{H}\,|\psi_{2e}\rangle$ correspond to the intradimer transfer integral (t_{d}). If we define the orbital energy level $\langle\psi_{1e}|\,\mathcal{H}\,|\psi_{2e}\rangle$ as 0, then the difference between the orbital energies is $\Delta\epsilon$. We can calculate the coefficients and intrinsic energy in case of Fig. 63 (c) as

follows:

$$|c_1|^2 = \frac{1}{2}\left(1 + \frac{\Delta\epsilon}{\sqrt{(\Delta\epsilon)^2 + 4(t_\mathrm{d})^2}}\right), \tag{17}$$

$$|c_2|^2 = \frac{1}{2}\left(1 - \frac{\Delta\epsilon}{\sqrt{(\Delta\epsilon)^2 + 4(t_\mathrm{d})^2}}\right), \tag{18}$$

$$E_\pm = \frac{\Delta\epsilon \pm \sqrt{(\Delta\epsilon)^2 + 4(t_\mathrm{d})^2}}{2}. \tag{19}$$

The extent of the charge transfer is given by $\Delta\rho = ||c_1|^2 - |c_2|^2|e$. Where e is the elementally charge. If we assume $\Delta\epsilon = 40$ meV [54], we obtain the charge transfer $\Delta\rho = +0.08e$, which is almost the same as the value of the charge transfer found by Hattori *et al.* [45]. Referring to their results, the extent of the charge transfer is independent of the magnitude of the applied electric field. This is also consistent with our model because the expected extent of charge transfer depends on only $\Delta\epsilon$ and t_d. We can thus explain the field-induced CD state both quantitatively and qualitatively in terms of the conformation changes of the ET molecules in the dimer. This mechanism is also consistent with the fact that this material shows no static electric dipole at low temperatures in the absence of an electric field. At low temperatures, the ethylene motion slows down, and almost all the ET molecules are likely to freeze into either the staggered or the eclipsed conformation [57, 70]. As a result, the CD state cannot occur in the absence of an electric field at low temperatures. However, if an electric field larger than $E = 5$ kV/cm is applied, an electric dipole moment p can be generated in the dimer accompanied by a conformation change of the ethylene group since the CD state is then realized. Once the conformation of ET changes, it is unlikely to return to the original conformation rapidly. Hence, the CD state can be maintained even if the applied electric field is removed.

14.5 Ethylene motion and the dielectric anomaly in β'-$(ET)_2ICl_2$

Finally, we discuss the possibility that the conformation change of ET molecules triggers the relaxor-like behavior in the dielectric constant of β'-$(ET)_2ICl_2$ salt [44]. As mentioned above, an electric dipole can be induced in a dimer if two ET molecules take different ethylene conformation from each other. In higher temperature region, the ethylene groups are thermally fluctuated very rapidly compared to the timescale of the permittivity measurement as shown in Fig. 57. Thus, the conformation changes are averaged over and the dipoles would not be produced in the dimers. Therefore, no anomaly

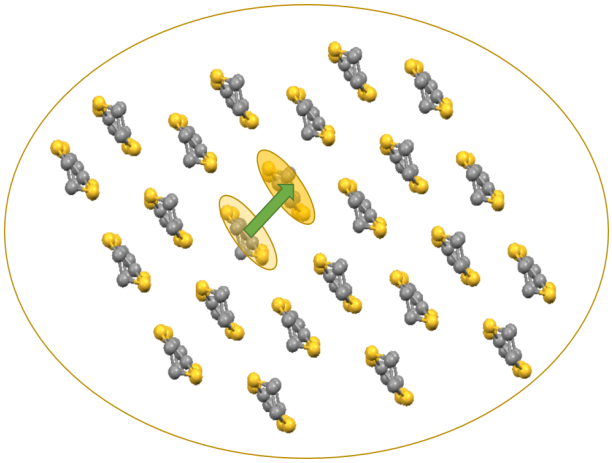

Figure 64: The schematic of domains which is possibly produced by the static dipole in a BEDT-TTF layer.

would be observed in the dielectric constant at higher temperature region. On the other hand, the permittivity measurement frequencies are much larger than the timescale of the ethylene motion around 100 K. In such case, the induced dipoles can be regarded as static ones. However, the static dipole in a dimer would produce a large-scale charge inhomogeneity and domains on the ET layers as shown in Fig. 64. They can respond to the applied electric fields and would result in the ferroelectric relaxor-like behavior. The formation of such ferroelectric domains is confirmed by Raman and polarization measurements [45]. In addition, it has been suggested that the domain structure plays a significant role for the relaxor-like anomaly in κ-$(ET)_2Cu_2CN_3$ salt. Note that the population of such dipoles would be small, therefore, the Raman scattering measurement under zero field cannot detect the charge inhomogeneity in a dimer. In contrast, almost all the ethylene groups may freeze with a thermally stable conformation either staggered or eclipsed in low temperature region as mentioned above [57, 70]. In this situation, there would also be no electric dipoles in the ET dimers and no anomaly in the electric constant would be appeared.

15 Summary for Part. III

In conclusion, we have performed ^{1}H-NMR and ^{13}C-NMR measurements for the dimer Mott insulator β'-$(ET)_2ICl_2$. Our ^{1}H-NMR measurements confirm the slowing down of the ethylene motion in β'-$(ET)_2ICl_2$. We have also confirmed the existence of significant

coupling between the ethylene motion and the electronic system of β'-$(ET)_2ICl_2$ by ^{13}C-NMR measurements. The ethylene motion modulates the molecular orbital of the ET molecules and affects the electronic state in the dimer. In addition, we have discussed a possible scenario for the emergence of an electric dipole in a dimer in terms of conformation changes of the ET molecules. Our model can explain the nature of both the field-induced CD state and the relaxor-like ferroelectric anomaly in the dielectric constant. Therefore, we propose that the slowing down of the ethylene motion can trigger the emergence of charge degrees of freedom and the dielectric anomaly in β'-$(ET)_2ICl_2$.

Acknowledgement

I would like to express my gratitude to Professor Atsushi Kawamoto, Professor Yoshihiro Ihara, and Professor Shuhei Fukuoka for their polite guidances and many advices. I would like to acknowledge Professor Noriaki Matsunaga, Professor Migaku Oda, Professor Tatsuya Yanagisawa and Professor Hiroyuki Yamase in the review process of my doctral thesis. I am grateful for the financial support given by Ushio Foundation. These studies were supported by Hokkaido University Global Facility Center (GFC), Advanced Physical Property Open Unit (APPOU), funded by MEXT under "Support Program for Implementation of New Equipment Sharing System" (JPMXS040100318). Finally, I would like to thank my family for their support.

References

[1] Takehiko Mori. *Bulletin of the Chemical Society of Japan*, 71:2509–2526, 1998.

[2] N. Drichko, M. Dressel, C. A. Kuntscher, A. Pashkin, A. Greco, J. Merino, and J. Schlueter. *Phys. Rev. B*, 74:235121, 2006.

[3] N. Yoneyama, A. Miyazaki, T. Enoki, , and G. Saito. *Bull. Chem. Soc. Jpn.*, 72:639, 1999.

[4] H. Kondo and T. Moriya. *Journal of the Physical Society of Japan*, 67:3695, 1998.

[5] J. Schmalian. *Physical Review Letters*, 81:4232, 1998.

[6] K. H. Bennemann and John B. Ketterson, editors. *Superconductivity*. Springer Berlin Heidelberg, Berlin, Heidelberg, 2008.

[7] R. H. McKenzie. *Science*, 278(5339):820–821, 1997.

[8] K Kanoda. *Hyperfine Interactions*, 104:235–249, 1997.

[9] Megumi Itaya, Yoshihiro Eto, Atsushi Kawamoto, and Hiromi Taniguchi. *Physical Review Letters*, 102:227003, 2009.

[10] H. Mori, M. Kamiya, H. Suzuki, M. Suto, S. Tanaka, Y. Nishio, K. Kajita, and H. Moriyama. *Journal of Physics and Chemistry of Solids*, 63:1239–1243, 2002.

[11] Takaaki Minamidate, Yuki Oka, Hironori Shindo, Toshitaka Yamazaki, Noriaki Matsunaga, Kazushige Nomura, and Atsushi Kawamoto. *Journal of the Physical Society of Japan*, 84:063704, 2015.

[12] Hisashi Tanaka, Akiko Kobayashi, Akane Sato, Hiroki Akutsu, and Hayao Kobayashi. *Journal of the American Chemical Society*, 121:760–768, 1999.

[13] Yohei Saito, Shuhei Fukuoka, Takuya Kobayashi, Atsushi Kawamoto, and Hatsumi Mori. *Journal of the Physical Society of Japan*, 87:013707, 2018.

[14] G E Pake. *The Journal of Chemical Physics*, 16:327–336, 1948.

[15] Hayao Kobayashi, Hideto Tomita, Takashi Udagawa, Toshio Naito, and Akiko Kobayashi. *Synthetic Metals*, 70:867–870, 1995.

[16] Shusaku Imajo, Satoshi Yamashita, Hiroki Akutsu, Hiroya Kumagai, Takuya Kobayashi, Atsushi Kawamoto, and Yasuhiro Nakazawa. *Journal of the Physical Society of Japan*, 88:023702, 2019.

[17] M. A. Tanatar, T. Ishiguro, S. Kagoshima, N. D. Kushch, and E. B. Yagubskii. *Physical Review B*, 65:064516, 2002.

[18] William A. Coniglio, Laurel E. Winter, Kyuil Cho, C. C. Agosta, B. Fravel, and L. K. Montgomery. *Physical Review B*, 83:224507, 2011.

[19] Shinya Uji, Kouta Kodama, Kaori Sugii, Taichi Terashima, Takahide Yamaguchi, Nobuyuki Kurita, Satoshi Tsuchiya, Takako Konoike, Motoi Kimata, Akiko Kobayashi, Biao Zhou, and Hayao Kobayashi. *Journal of the Physical Society of Japan*, 84:104709, 2015.

[20] Hayao Kobayashi, Hideto Tomita, Toshio Naito, Akiko Kobayashi, Fumiko Sakai, Tokuko Watanabe, and Patrick Cassoux. *Journal of the American Chemical Society*, 118:368–377, 1996.

[21] S. Uji, H. Shinagawa, T. Terashima, T. Yakabe, Y. Terai, M. Tokumoto, A. Kobayashi, H. Tanaka, and H. Kobayashi. *Nature*, 410:908–910, 2001.

[22] Hisashi Tanaka, Takafumi Adachi, Emiko Ojima, Hideki Fujiwara, Kiyonori Kato, Hayao Kobayashi, Akiko Kobayashi, and Patrick Cassoux. *Journal of the American Chemical Society*, 121:11243–11244, 1999.

[23] T. Kobayashi, T. Ishikawa, A. Ohnuma, M. Sawada, N. Matsunaga, H. Uehara, and A. Kawamoto. *Physical Review Research*, 2:023075, 2020.

[24] T. Kobayashi and A. Kawamoto. *Physical Review B*, 96:125115, 2017.

[25] D. Jérome. *Science*, 252:1509–1514, 1991.

[26] Yoshitaka Kimura, Masaki Misawa, and Atsushi Kawamoto. *Physical Review B*, 84:045123, 2011.

[27] Hayao Kobayashi, Takashi Udagawa, Hideto Tomita, Kozo Bun, Toshio Naito, and Akiko Kobayashi. *Chemistry Letters*, 22:1559–1562, 1993.

[28] Takuma Kawai and Atsushi Kawamoto. *Journal of the Physical Society of Japan*, 78:074711, 2009.

[29] Toru Moriya and Kazuo Ueda. *Reports on Progress in Physics*, 66:1299–1341, 2003.

[30] Yohei Saito and Atsushi Kawamoto. *Solid State Nuclear Magnetic Resonance*, 73:22–30, 2016.

[31] S. S. Saxena, K. Ahilan, T. E. Weller, M. Ellerby, R. P. Smith, N. T. Skipper, S. Rowley, A. Kusmartseva, and G. G. Lonzarich. *Iranian Journal of Physics Research*, 6:129, 2006.

[32] P. M. Grant. *Journal de Physique Paris*, 44:C3–847, 1983.

[33] K. Oshima, Takehiko Mori, H. Inokuchi, H. Urayama, H. Yamochi, and Gunzi Saito. *Physical Review B*, 38:938–941, 1988.

[34] L.K. Montgomery, T. Burgin, J.C. Huffman, J. Ren, and M.-H. Whangbo. *Physica C: Superconductivity*, 219:490–496, 1994.

[35] Charles Mielke, John Singleton, Moon-Sun Nam, Neil Harrison, C C Agosta, B Fravel, and L K Montgomery. *Journal of Physics: Condensed Matter*, 13:8325–8345, 2001.

[36] Nicolas Doiron-Leyraud, Pascale Auban-Senzier, Samuel René de Cotret, Claude Bourbonnais, Denis Jérome, Klaus Bechgaard, and Louis Taillefer. *Physical Review B*, 80:214531, 2009.

[37] H. v. Löhneysen, A Rosch, M. Vojta, and P. Wölfe. *Reviews of Modern Physics*, 79:1015, 2007.

[38] S. Ishihara. *J. Phys. Soc. Jpn.*, 79:011010, 2010.

[39] M. Naka and S. Ishihara. *J. Phys. Soc. Jpn.*, 79:063707, 2010.

[40] K. Kobayashi, S. Horiuchi, R. Kumai, F. Kagawa, Y. Murakami, and Y. Tokura. *Phys. Rev. Lett.*, 108:237601, 2012.

[41] J. B. Torrance, J. E. Vazquez, J. J. Mayerle, and V. Y. Lee. *Phys. Rev. Lett.*, 46:253, 1981.

[42] F. Nad, P. Monceau, C. Carcel, and J. M. Fabre. *Phys. Rev. B*, 62:1753, 2000.

[43] P. Monceau, F. Ya Nad, and S. Brazovskii. *Phys. Rev. Lett.*, 86:4080–4083, 2001.

[44] S. Iguchi, S. Sasaki, N. Yoneyama, H. Taniguchi, T. Nishizaki, and T. Sasaki. *Phys. Rev. B*, 87:075107, 2013.

[45] Y. Hattori, S. Iguchi, T. Sasaki, S. Iwai, H. Taniguchi, and H. Kishida. *Phys. Rev. B*, 95:085149, 2017.

[46] Majed Abdel-Jawad, Ichiro Terasaki, Takahiko Sasaki, Naoki Yoneyama, Norio Kobayashi, Yoshiaki Uesu, and Chisa Hotta. *Physical Review B*, 82:125119, 2010.

[47] M. Abdel-Jawad, N. Tajima, R. Kato, and I. Terasaki. *Phys. Rev. B*, 88:075139, 2013.

[48] M. Dressel, P. Lazić, A. Pustogow, E. Zhukova, B. Gorshunov, J. A. Schlueter, O. Milat, B. Gumhalter, and S. Tomić. *Physical Review B*, 93:081201, 2016.

[49] Hayao Kobayashi, Reizo Kato, Akiko Kobayashi, Gunzi Saito, Madoka Tokumoto, Hiroyuki Anzai, and Takehiko Ishiguro. *Chemistry Letters*, 15:89–92, 1986.

[50] H. Taniguchi, K. Kanoda, and Atsushi Kawamoto. *Physical Review B*, 67:1–5, 2003.

[51] Hiori Kino and Hidetoshi Fukuyama. *Journal of the Physical Society of Japan*, 65:2158–2169, 1996.

[52] Yoshihiro Eto and Atsushi Kawamoto. *Physical Review B*, 81:020512, 2010.

[53] T. Yamamoto, M. Uruichi, K. Yamamoto, K. Yakushi, A. Kawamoto, and H. Taniguchi. *J. Phys. Chem.*, 109:15226, 2005.

[54] Yuki Kuwata, Megumi Itaya, and Atsushi Kawamoto. *Physical Review B*, 83:144505, 2011.

[55] Miko Matsumoto, Yohei Saito, and Atsushi Kawamoto. *Physical Review B*, 90:115126, 2014.

[56] Urs Geiser, Arthur J. Schults, Hau H Wang, Diana M Watkins, Daniel L Stupka, Jack M Williams, J.E. Schirber, D.L. Overmyer, D. Jung, J.J. Novoa, and M.-H. Whangbo. *Physica C: Superconductivity*, 174:475–486, 1991.

[57] Daniel Guterding, Roser Valentí, and Harald O. Jeschke. *Physical Review B*, 92:081109, 2015.

[58] K. Murata, M. Tokumoto, H. Anzai, Y. Honda, N. Kinoshita, T. Ishiguro, Naoki Toyota, T. Sasaki, and Y. Muto. *Synthetic Metals*, 27:A263–A270, 1988.

[59] T Takahashi, T Tokiwa, K Kanoda, H Urayama, H Yamochi, and G Saito. *Synthetic Metals*, 27:A319–A324, 1988.

[60] K. Miyagawa, Atsushi Kawamoto, Y. Nakazawa, and K Kanoda. *Physical Review Letters*, 75:1174–1177, 1995.

[61] Yutaka Maniwa, Toshihiro Takahashi, and Gunzi Saito. *Journal of the Physical Society of Japan*, 55:47–50, 1986.

[62] N. Bloembergen, E. M. Purcell, and R. V. Pound. *Physical Review*, 73:679–712, 1948.

[63] H. Taniguchi, R. Sato, K. Satoh, A. Kawamoto, H. Okamoto, T. Kobayasi, and K. Mizuno. *J. Low Temp. Phys.*, 142:437–440, 2006.

[64] M Yamashita, Atsushi Kawamoto, and K Kumagai. *Synthetic Metals*, 133-134:125–127, 2003.

[65] Shinji Hirose, Masaki Misawa, and Atsushi Kawamoto. *Crystals*, 2:1034–1057, 2012.

[66] C. P. Slichter. *Principles of magnetic reasonance.* Berlin:Sprinter-Verlag Berlin Heidelberg, 1990.

[67] Edan Scriven and B. J. Powell. *Physical Review B - Condensed Matter and Materials Physics*, 80:1–9, 2009.

[68] T. Koretsune and C. Hotta. *Phys. Rev. B*, 89:045102, 2014.

[69] K. Hashimoto, R. Kobayashi, H. Okamura, H. Taniguchi, Y. Ikemoto, T. Moriwaki, S. Iguchi, M. Naka, S. Ishihara, and T. Sasaki. *Physical Review B*, 92:085149, 2015.

[70] Xiaohong Wang, Chuansheng Ge, Xuechao Xing, Ping Wang, Daming Zhang, Peiji Wu, and Daoben Zhu. *Synthetic Metals*, 39:355–358, 1991.